

See discussions, stats, and author profiles for this publication at: <https://www.researchgate.net/publication/307549605>

Discrete-Fracture Modeling of Complex Hydraulic-Fracture Geometries in Reservoir Simulators

Article in *SPE Reservoir Evaluation & Engineering* · August 2016

DOI: 10.2118/183647-PA

CITATIONS

10

READS

280

4 authors, including:



Yifei Xu

University of Texas at Austin

10 PUBLICATIONS 25 CITATIONS

SEE PROFILE



Jose Sergio de Araújo Cavalcante Filho

Petróleo Brasileiro S.A.

5 PUBLICATIONS 11 CITATIONS

SEE PROFILE



Wei Yu

Texas A&M University

81 PUBLICATIONS 646 CITATIONS

SEE PROFILE

Some of the authors of this publication are also working on these related projects:



Embedded Discrete Fracture Model [View project](#)



Fishbone Modeling [View project](#)

All content following this page was uploaded by [Wei Yu](#) on 01 September 2016.

The user has requested enhancement of the downloaded file.

Discrete-Fracture Modeling of Complex Hydraulic-Fracture Geometries in Reservoir Simulators

Y. Xu, University of Texas at Austin; J. S. A. Cavalcante Filho, Petrobras; W. Yu, Texas A&M University; and K. Sepehrnoori, University of Texas at Austin

Summary

Hydraulic fracturing is a dominant technology in unconventional resources development. Recent advances in fracture-diagnostic tools and fracture-propagation models make it necessary to model fractures with complex geometries in reservoir-simulation studies.

In this paper, we present an efficient method to model fractures with complex geometries with reservoir simulators. Through non-neighboring connections (NNCs), an embedded discrete-fracture modeling (EDFM) formulation is applied to reservoir simulators to properly model fractures with complex geometries such as fracture networks and nonplanar hydraulic fractures. We demonstrate the accuracy of the approach by performing a series of case studies with two commercial reservoir simulators and comparing the results with local-grid-refinement (LGR) models and a semianalytical solution. The limitations of the model are also discussed. In addition, the results show its computational efficiency as the complexity of fractures increases. We also present two numerical case studies to demonstrate the applicability of our method in naturally fractured reservoirs.

The nonintrusive application of the EDFM allows insertion of the discrete fractures into the computational domain and the use of original functionalities of the simulators without having access to the source code of the simulators. It may be easily integrated into existing frameworks for unconventional reservoirs to perform sensitivity analysis, history matching, and production forecasting.

Introduction

The advanced technologies of horizontal drilling and multistage hydraulic fracturing have gained great success in economic development of unconventional oil and gas reservoirs. Also, some related techniques such as fracture diagnostics, fracture-propagation modeling, and unconventional-reservoir simulation have been developed further to provide a comprehensive framework for optimization of the unconventional-resources development.

Fracture-diagnostic tools, such as microseismic and distributed temperature sensing, provide valuable information for fracture characterization and monitoring, indicating that complex fracture-networks are often generated during hydraulic-fracturing operations because of the pre-existing natural fractures (Maxwell et al. 2002; Fisher et al. 2004; Gale et al. 2007; Warpinski et al. 2009; Cipolla et al. 2010). Furthermore, experimental studies have shown that the shape of a single hydraulic fracture can also be complex [e.g., nonplanar fracture with variable aperture (Abass et al. 1996; El-Rabaa 1989; Weijers and de Pater 1992)]. Recent developments in fracture-propagation modeling also indicate that irregular hydraulic-fracture shapes are originated caused by the “stress-shadow” effect or the influence of natural-fracture networks (Olson 2008; Weng et al. 2011; Wu and Olson 2014, 2015).

Because the presence of fractures significantly affects the flow behavior, it is important to accurately model the influence of fractures on well performance. However, it is still a challenging problem to model realistic fractures with complex geometries

for production analysis. Extensive work has been conducted to solve this problem analytically (Zhou et al. 2014; Yu 2015) and numerically (Hoteit and Firoozabadi 2006; Marcondes et al. 2010).

In simulators, dual-porosity and dual-permeability approaches are not adequate for modeling complex fractures and capturing the influence of fracture connectivity. Discrete-fracture models (DFMs), using finite-element or finite-difference methods, have been developed to overcome such problems. Unstructured grids are used in most discrete-fracture modeling (Noorishad and Mehran 1982; Karimi-Fard and Firoozabadi 2003; Monteagudo and Firoozabadi 2004; Matthai et al. 2005; Hoteit and Firoozabadi 2006; Sandve et al. 2012; Hui et al. 2013) to explicitly model the fractures. Irregular fracture-shapes, such as nonplanar fractures and fractures with variable aperture, can also be represented through appropriate gridding around the fractures (Karimi-Fard et al. 2004; Al-Hinai et al. 2013; Olorode et al. 2013). However, the use of unstructured grids in real field studies is still limited because of its complexity in gridding and computational cost.

As a compromise, the EDFM was developed (Lee et al. 2001; Li and Lee 2008; Hajibeygi et al. 2011) to honor the accuracy of DFMs while keeping the efficiency offered by structured gridding. In this approach, the reservoir is discretized with Cartesian grids, and additional cells are introduced for fractures. The influence of fractures is explicitly modeled through a transport index between nonneighboring cells. Moinfar et al. (2014) extended the EDFM for 3D simulations to include slanted fractures, and implemented the method in an in-house compositional reservoir simulator. Later, Cavalcante Filho et al. (2015) developed a pre-processing code for general transport-index calculations. As an extension of the EDFM, Panfili and Cominelli (2014) applied the EDFM to a commercial simulator and performed case studies with corner-point geometry grids. Jiang et al. (2014) integrated the EDFM with dual-continuum and MINC (multiple interacting continua) to model the fracture network in a shale gas reservoirs.

In the previous applications of the EDFM, fractures with nonplanar shapes or variable apertures were not modeled in a nonintrusive way to introduce the EDFM into reservoir simulators. Also, there is no detailed analysis of the computational performance of the EDFM. Lack of such work makes it difficult for the EDFM to become a widely used approach in unconventional-reservoir simulation.

In this paper, we first describe a general method to introduce the EDFM into reservoir simulators with Cartesian grids. Then, the calculation procedure for the transport indices in the EDFM is introduced, and the limitations are discussed. The methodology to model fractures with nonplanar shape and variable aperture is also presented. Subsequently, through a series of case studies with two commercial reservoir simulators, we demonstrate the applicability of the EDFM in modeling of complex fracture-networks and irregular fracture-shapes. The accuracy and computational efficiency of the EDFM are also demonstrated through comparison with LGR model and a semianalytical solution. Finally, we perform a field case study to show a potential application of the EDFM in a hydraulically fractured reservoir with natural fractures.

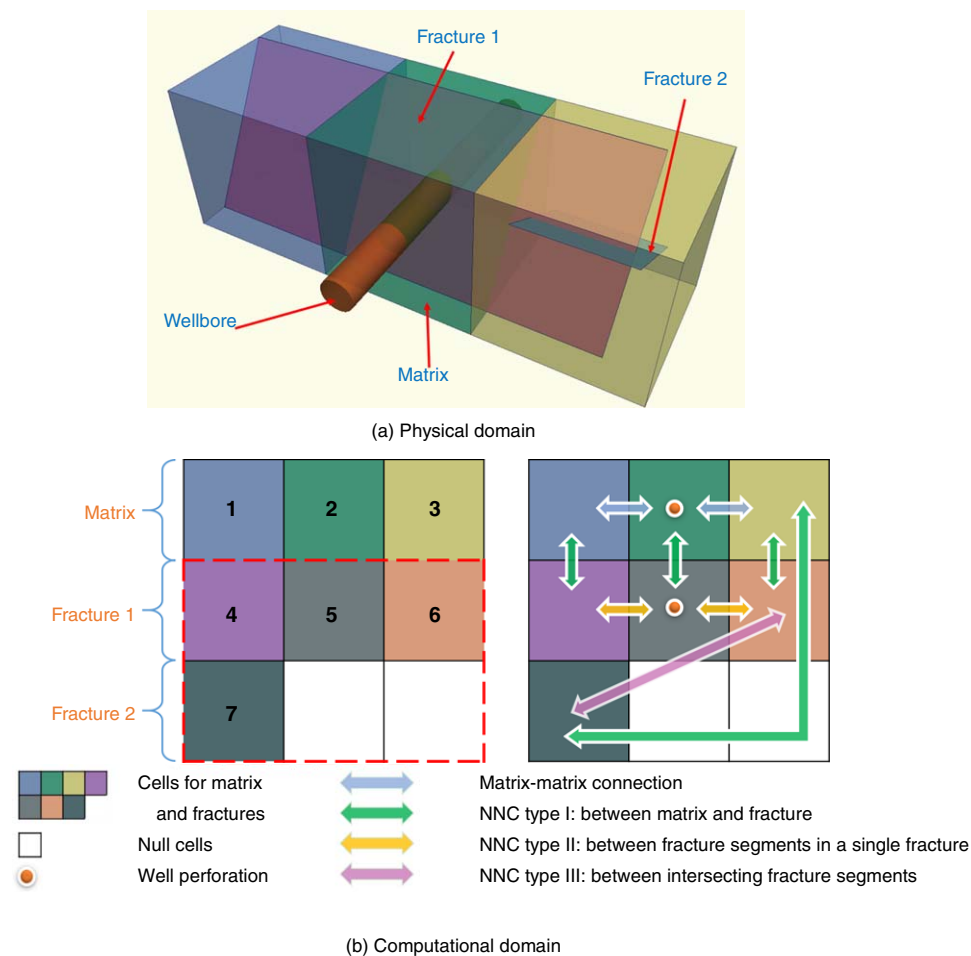


Fig. 1—Explanation of the EDFM. In (a), we show a case with three matrix blocks, two fractures, and a wellbore in the physical domain. In (b), we show the corresponding cells in the computational domain, and the arrows show different types of connections.

EDFM in Conventional Finite-Difference Reservoir Simulator

The EDFM borrows the concept from the dual-continuum approach that creates fracture cells in contact with corresponding matrix cells to account for the mass transfer between continua. After a fracture penetrates a matrix cell, an additional cell is created to represent the fracture segment in the physical domain. Each individual fracture could be discretized into several fracture segments by the matrix-cell boundaries. To differentiate the newly added cells from the original matrix cells, these additional cells are called fracture cells.

In Fig. 1, we illustrate the procedure to add fracture cells in the EDFM with a simple case with only 3 matrix blocks and 2 fractures. Fig. 1a shows the physical domain and Fig. 1b shows the computational domain. Each matrix block or fracture segment in the physical domain is represented by a cell in the computational domain with the same color. Before adding the fractures, we have 3 matrix cells: Cell 1, Cell 2, and Cell 3. After adding the fractures, the total number of cells increases. Fracture 1 penetrates all three matrix blocks; hence, three fracture cells (Cells 4, 5, and 6) are introduced into the computational domain to represent the corresponding fracture segments. Similarly, only one extra cell (Cell 7) is added for Fracture 2 because it only penetrates one matrix block. Because we use structured grid, every row should have the same number of cells; therefore, 2 null cells are also introduced. Finally, the total number of cells increases from 3 ($1 \times 3 = 3$) to 9 ($3 \times 3 = 9$). The depth of each fracture cell is defined as the depth of the centroid of the corresponding fracture segment. In addition, we assign an effective porosity for each fracture cell to maintain the pore volume (PV) of the fracture segment,

$$\phi_f = \frac{S_{seg} w_f}{V_b}, \quad \dots \quad (1)$$

where ϕ_f is the effective porosity for a fracture cell, S_{seg} is the area of the fracture segment perpendicular to the fracture aperture, w_f is the fracture aperture, and V_b is the bulk volume of the cell assigned for the fracture segment.

After adding cells to represent fracture segments, we cancel the connections automatically generated by the simulator for these cells. NNCs are subsequently defined. The aim for introducing NNCs is to allow flow communication between cells that are physically connected but not neighboring in the computational domain. Three types of NNCs are defined as follows:

- NNC Type I: connection between a fracture segment and the matrix block it penetrates
- NNC Type II: connection between fracture segments in same fracture
- NNC Type III: connection between intersecting fracture segments

All three types of NNCs are shown by arrows in Fig. 1b. The cells in each NNC pair are connected by transmissibility factors. The NNC pairs and transmissibility factors are provided by a preprocessor.

In addition to these NNCs, the connections between fractures and wells are also introduced by the EDFM. When a fracture segment intersects the wellbore trajectory (as shown in Fig. 1a), we define the corresponding fracture cell as a wellblock by adding a well perforation for this cell, as shown in Fig. 1b.

This general procedure can be used in different reservoir simulators. As a nonintrusive method, the calculations of the connection factors, including NNC transmissibility factor and fracture-

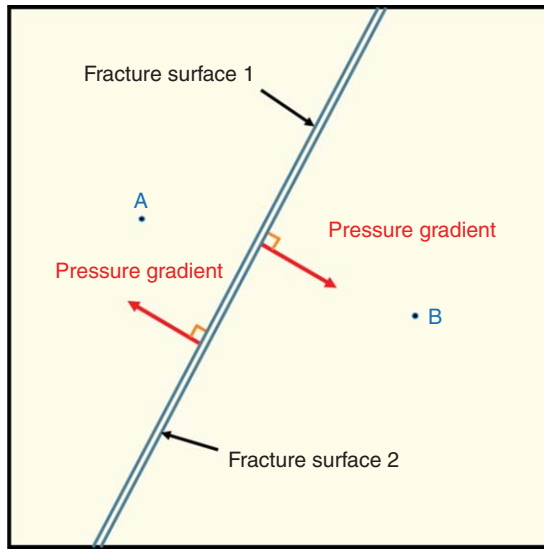


Fig. 2—Illustration of the connection between matrix cell and fracture segment.

well index, depend only on the gridding, reservoir permeability, and fracture geometries. Details of the calculations will be discussed in next section. We developed a general-purpose EDFM preprocessor on the basis of Cavalcante Filho et al. (2015)'s work for all those geometrical calculations. The preprocessor was developed in Python and Fortran programming languages. Taking the reservoir and gridding information as inputs, the EDFM preprocessor provides information such as the number of extra grids, the equivalent properties of these grids, and the NNC pairs to help users make changes in the simulation input.

Calculation of NNC Transmissibility and Fracture Well-Index

This section presents a brief review of the formulations to calculate the connection factors. The proposed formulations here are mainly on the basis of two-point flux approximation. The assumptions and limitations are also discussed. The EDFM preprocessor only calculates the phase-independent part of the connection factors, and the phase-dependent part is calculated by the simulator.

Matrix–Fracture Connection. The NNC transmissibility factor between matrix and fracture segment depends on the matrix permeability and fracture geometry. When a fracture segment fully penetrates a matrix cell, if we assume a uniform pressure gradient in the matrix cell and that the pressure gradient is normal to the fracture plane as shown in **Fig. 2**, the matrix–fracture transmissibility factor is

$$T_{f-m} = \frac{2A_f(K \cdot \vec{n}) \cdot \vec{n}}{d_{f-m}}, \quad \dots \quad (2)$$

where A_f is the area of the fracture segment on one side, K is the matrix-permeability tensor, \vec{n} is the normal vector of the fracture plane, and d_{f-m} is the average normal distance from matrix to fracture, which is calculated as

$$d_{f-m} = \frac{\int_V x_n dV}{V}, \quad \dots \quad (3)$$

where V is the volume of the matrix cell, dV is the volume element of matrix, and x_n is the distance from the volume element to the fracture plane. Detailed derivation of Eq. 2 can be found in Appendix A.

If the fracture does not fully penetrate the matrix cell, the calculation of the transmissibility factor is complex because the pres-

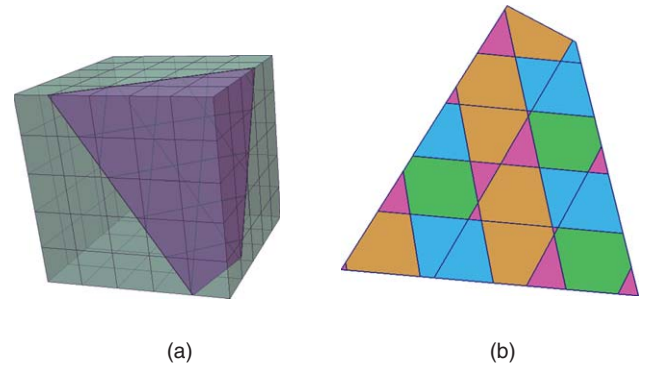


Fig. 3—An example of different shapes of fracture segments in an individual fracture. The fracture is cut into 29 segments by the cell boundaries shown in (a). In (b), the segments are colored on the basis of their number of vertices. They can be triangular, quadrilateral, pentagonal, or hexagonal.

sure distribution in the matrix cell may deviate from the previous assumptions. To make the method nonintrusive, we make the same assumption as Li and Lee (2008) that the transmissibility factor is proportional to the area of the fracture segment inside the matrix cell.

Connection Between Fracture Segments in an Individual Fracture. In the EDFM, a fracture can be discretized into many segments with different shapes, including triangular, quadrilateral, pentagonal, and hexagonal, as shown in **Fig. 3**. Thus, the connection between these segments is a 2D unstructured grid problem. Here, to make it easier to be handled by traditional reservoir simulators, we adopt a simplified approximation similar to Karimi-Fard et al. (2004). The transmissibility factor between a pair of neighboring Segments 1 and 2 is evaluated with a two-point flux-approximation scheme as

$$T_{\text{seg}} = \frac{T_1 T_2}{T_1 + T_2}, \quad \dots \quad (4a)$$

$$T_1 = \frac{k_f A_c}{d_{\text{seg1}}}, T_2 = \frac{k_f A_c}{d_{\text{seg2}}}, \quad \dots \quad (4b)$$

where k_f is the fracture permeability, A_c is the area of the common face for these two segments, and d_{seg1} and d_{seg2} are the distances from the centroids of Segments 1 and 2 to the common face, respectively. This two-point flux approximation scheme will lose some accuracy for 3D cases in which the fracture segments may not form orthogonal grids. When the flow in the fracture plane becomes vital for the total flow, a multipoint flux approximation may be more appropriate, which will be discussed in our future publications.

Fracture Intersection. Accurate and efficient modeling of fracture intersection is a challenging problem for discrete-fracture modeling. The complexity of flow behavior at the fracture intersection makes it difficult to be modeled accurately. Here, we follow the work of Moinfar et al. (2014) to simplify this problem by assigning a transmissibility factor between intersecting fracture segments to approximate the mass transfer at the fracture intersection. The transmissibility factor is calculated as

$$T_{\text{int}} = \frac{T_1 T_2}{T_1 + T_2}, \quad \dots \quad (5a)$$

$$T_1 = \frac{k_{f1} w_{f1} L_{\text{int}}}{d_{f1}}, T_2 = \frac{k_{f2} w_{f2} L_{\text{int}}}{d_{f2}}, \quad \dots \quad (5b)$$

where L_{int} is the length of the intersection line and d_{f1} and d_{f2} are the weighted average of the normal distances from the centroids of the subsegments (on both sides) to the intersection line. In **Fig. 4**,

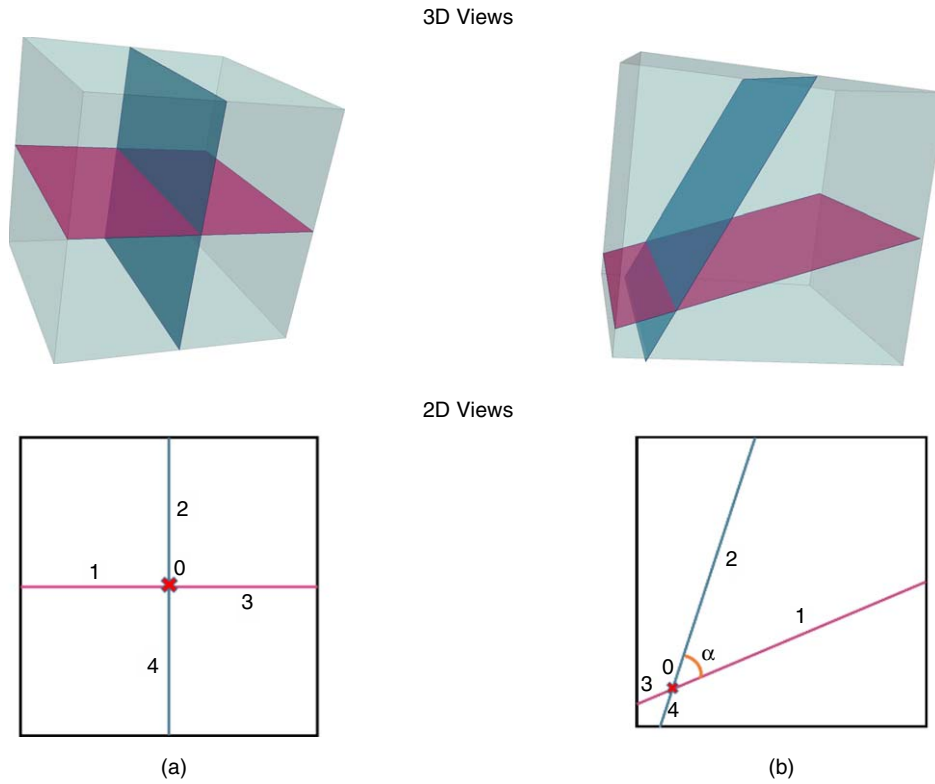


Fig. 4—Explanation of fracture intersection. At intersection, every fracture segment will be divided into 2 subsegments. In (a), all the subsegments have similar dimensions. In (b), there is a high contrast between areas of the subsegments.

$$d_{f1} = \frac{\int_{S_1} x_n dS_1 + \int_{S_3} x_n dS_3}{S_1 + S_3}$$

$$d_{f2} = \frac{\int_{S_2} x_n dS_2 + \int_{S_4} x_n dS_4}{S_2 + S_4}, \quad \dots \dots \dots (6)$$

where dS_i is the area element, S_i is the area of the fracture subsegment i , and x_n is the distance from the area element to the intersection line. It is not necessary to perform integrations for the average normal distance. Because the subsegments are always polygonal, the geometrical method can be used to speed up the calculation.

The limitation of this fracture-intersection model is that it cannot consider the complex flow mechanisms at the fracture intersection such as stream-tube routing (Berkowitz et al. 1994) because the flow direction in each subsegment is unknown. The influence of intersection angle is not considered either. Therefore, for multicomponent flow with high local Péclet number ($Pe > 10^{-2}$) (Berkowitz et al. 1994), Eq. 6 should be used with caution.

Well–Fracture Intersection. We model the well–fracture intersections in the EDFM by assigning an effective well index for the fracture segments that intersect the well trajectory. The most commonly used formula proposed by Peaceman (1983) is applied here (Moinfar et al. 2013):

$$WI_f = \frac{2\pi k_f w_f}{\ln\left(\frac{re}{rw}\right)}, \quad re = 0.14\sqrt{L_S^2 + H_S^2}, \quad \dots \dots \dots (7)$$

where k_f is the fracture permeability, w_f is the fracture aperture, L_S is the length of the fracture segment, H_S is the height of the fracture segment, re is the effective radius, and rw is the wellbore radius.

Modeling of Complex Fracture Geometries

Nonplanar-Fracture Geometry. Mathematically, the preprocessor calculates the intersection between a plane (fracture) and a cuboid (matrix cell). To account for the complexity in fracture shape, we extend the EDFM to handle nonplanar fracture shape by discretizing a nonplanar fracture into several interconnected planar fractures. The connections between these planar-fracture segments are treated as fracture intersections.

For two intersecting fracture segments, if two subsegments have small areas (as shown in Fig. 4b, $S_3 \rightarrow 0$, $S_4 \rightarrow 0$), the transmissibility factor between the fracture segments is mainly determined by subsegments with larger areas. In Eq. 6, we will have

$$d_{f1} = \frac{\int_{S_1} x_n dS_1}{S_1}, \quad d_{f2} = \frac{\int_{S_2} x_n dS_2}{S_2}. \quad \dots \dots \dots (8)$$

The formula for this transmissibility-factor calculation (T_{int}) has the same form as the one used for the two fracture segments in an individual fracture (T_{seg}), if the permeability and the aperture of the two intersecting fractures are the same. This approach is used to model nonplanar fractures. Fig. 5 illustrates how a nonplanar fracture is dealt with using the EDFM. The fracture in the figure is discretized into six interconnected planar fractures. For each intersection, the ratios of L1/L3 and L2/L4 should be high enough to eliminate the influence of the small subsegments. In this study, the ratios are set as 100.

Fractures With Variable Aperture. A fracture with variable apertures can be modeled with the EDFM by discretizing it into some connecting segments and assigning each segment an “average aperture” (\bar{w}_f) and “effective permeability” ($k_{f,eff}$). Attention needs to be paid to determine both parameters.

Fig. 6 shows a 2D case in which a fracture segment has a length of L_S with variable aperture and x is the distance from a cross section to one end of the fracture segment. The aperture is a function of x . The total volume of the segment is

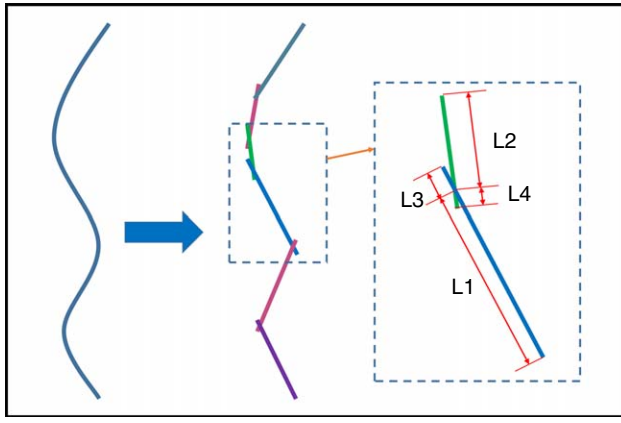


Fig. 5—Illustration of the modeling of nonplanar fracture.

$$V_{\text{seg}} = H \int_0^{L_s} w_f(x) dx, \quad \dots \dots \dots (9)$$

where H is the height of the fracture segment. The average aperture to calculate the volume should be

$$\bar{w}_f = V_{\text{seg}} / HL_s = \frac{1}{L_s} \int_0^{L_s} w_f(x) dx. \quad \dots \dots \dots (10)$$

For transmissibility calculation, if we assume the cubic law for fracture conductivity,

$$C_f(x) = k_f(x)w_f(x) = \lambda w_f^3(x), \quad \dots \dots \dots (11)$$

where λ is 1/12 for smooth fracture surfaces and $\lambda < 1/12$ for coarse fracture surface.

For the fluid flow in fractures, on the basis of Darcy's law,

$$Q_j = HC_f(x)\lambda_j \frac{dP}{dx}, \quad \dots \dots \dots (12)$$

where Q_j is flow rate of phase j and λ_j is the relative mobility of phase j . For each fracture segment, if we assume constant Q_j , the pressure drop along the fracture segment is

$$\Delta p = \int_0^{L_s} \frac{Q_j}{HC_f(x)} dx. \quad \dots \dots \dots (13)$$

To keep the pressure drop constant between both ends of the segments, an effective fracture conductivity can be defined that satisfies the following equation:

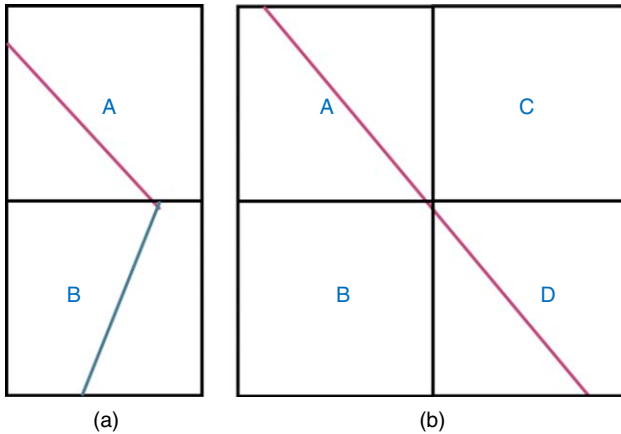


Fig. 7—The 2D examples showing the influence of small fracture segment. The red and blue lines represent the fracture segments. In both (a) and (b), removing the fracture segment in Cell B will lead to loss of connectivity.

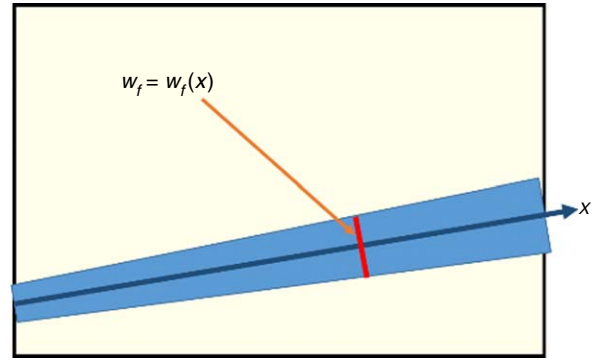


Fig. 6—A 2D example showing a fracture segment with varying aperture.

$$\int_0^{L_s} \frac{Q_j}{HC_f(x)} dx = \int_0^{L_s} \frac{Q_j}{HC_f^{\text{eff}}(x)} dx, \quad \dots \dots \dots (14)$$

which gives

$$C_f^{\text{eff}} = \frac{L_s}{\int_0^{L_s} \frac{dx}{C_f(x)}} = \frac{L_s}{\int_0^{L_s} \frac{dx}{\lambda w_f^3(x)}}. \quad \dots \dots \dots (15)$$

Because the fracture conductivity is the product of fracture aperture and fracture permeability, if \bar{w}_f is used for the whole fracture segment, an effective fracture permeability $k_{f,\text{eff}}$ is required to calculate the conductivity

$$k_{f,\text{eff}} = C_f^{\text{eff}} / \bar{w}_f = \frac{L_s^2}{\left[\int_0^{L_s} w_f(x) dx \right] \left[\int_0^{L_s} \frac{dx}{\lambda w_f^3(x)} \right]}. \quad \dots \dots \dots (16)$$

Similarly, if we assume constant fracture permeability but varying aperture, the effective fracture permeability should be

$$k_{f,\text{eff}} = \frac{L_s^2}{\left[\int_0^{L_s} w_f(x) dx \right] \left[\int_0^{L_s} \frac{dx}{k_f w_f(x)} \right]}. \quad \dots \dots \dots (17)$$

Special Handling of Extra-Small Fracture Segments. In the EDFM, the discretization of fractures by cell boundaries may generate some fracture segments with extremely small volumes. The upper-left segment in Fig. 3b is an example. This happens more frequently when modeling complex fracture geometries, in which many small fractures are used to represent the nonplanar shape and variation in aperture. These small control-volumes may cause problems in preconditioning, and they limit the simulation timestep to an unreasonable value. Simply eliminating these segments may cause the loss of connectivity, as shown in **Fig. 7**. A star-delta method (Karimi-Fard et al. 2004) can be used to prevent such problems and increase the stability of the EDFM. For a fracture segment with extra-small volume, if N denotes the number of NNCs related to this fracture segment, C_1, C_2, \dots, C_N denote the cells connected to this segment by NNCs, and T_1, T_2, \dots, T_N denote the NNC transmissibility factors related to these connections, then, the small segment can be eliminated following the steps given next:

1. Remove the cell for this segment in computational domain. Then, eliminate all NNCs related to this cell.
2. Add $N(N-1)/2$ connections for any pair of cells in C_1, C_2, \dots, C_N , and the transmissibility factor between C_i and C_j is

$$T_{i-j} = \frac{T_i T_j}{\sum_{k=1}^N T_k}. \quad \dots \dots \dots (18)$$

Parameter	Value	Unit
Reservoir permeability	0.0005	md
Reservoir porosity	12%	—
Initial reservoir pressure	4,500	psi
Reservoir thickness	80	ft
Rock compressibility	1×10^{-6}	psi ⁻¹
Initial water saturation	10%	—
Initial gas saturation	90%	—
Depth of top layer	1,000	ft
Langmuir pressure	535	psi
Langmuir volume	196.4	scf/ton
Rock density	164.2	lbm/ft ³
Bottomhole pressure	1,000	psi
Wellbore radius	0.25	ft
Simulation time	1,000	days

Table 1—Basic reservoir and operation parameters in simulations for Case 1.

The previous method eliminates the small control-volumes while keeping the appropriate connectivity. However, because only the phase-independent part of transmissibility is considered in the transformation, for multiphase flow, this method is only an approximation (Karimi-Fard et al. 2004). Furthermore, it cannot be applied to fracture segments with well intersections because it will cause loss of fracture-well connection. Therefore, for multiphase flow and fracture wellblocks, this method is not recommended. Furthermore, because this method ignores the volume of the small fracture segments, it is recommended only when a very high PV contrast (e.g., 1,000) between fracture cells exists.

Model Verifications

In the following simulation studies, we present five cases to demonstrate the applicability of the EDFM. As stated previously, the EDFM is a nonintrusive method that may be used in any finite-difference reservoir simulator capable of handling NNCs. Therefore, the range of problems that our method can handle and the

physics involved depend mainly on the capability of the simulator. The EDFM is applicable in both 2D and 3D cases, for both compositional and black-oil formulations. In this study, two commercial reservoir simulators (referred as RS1 and RS2) were used to perform the case studies. We show the results of RS1 in all cases, and the results obtained with RS2 are compared with the results of RS1. The examples consider shale gas (methane) production from a multifractured horizontal well. Water is at residual saturation, and the only flowing phase is gas. The gas relative permeability at residual water saturation is assumed to be 1.0, and no capillary effect is considered. Two dimensional reservoir models are used for verification purposes. We used black-oil formulations to avoid the differences between compositional calculations in simulators. Most of the reservoir properties and operation parameters were kept the same for all five cases, as shown in Table 1. The Langmuir gas-desorption effect was considered following the method of Seidle and Arri (1990). The detailed formulation and revised pressure/volume/temperature (PVT) table are given in Appendix B. We demonstrate the accuracy of our model by comparing the gas-flow rates and pressure profiles of the EDFM with the LGR models or a semi-analytical solution, which is briefly introduced in Appendix C. In the LGR models, only the cells containing fractures are refined (into three subcells in the direction perpendicular to the fracture plane) to speed up the simulations, as shown in Fig. 8. The coarse grids in both EDFM and LGR models are kept the same in each case to make fair comparison in CPU time. The apertures of the fractures are modeled as the real sizes, for example, 0.015 feet.

Case 1: Biwing Fractures. We first consider an ideal case with four transverse planar fractures perpendicular to the wellbore. The reason why we choose this case is that most simulators can handle this case accurately through LGR. The reservoir is rectangular with dimensions of $3,100 \times 1,675 \times 80$ ft, and it is discretized by 200×99 gridblocks horizontally. The fracture half-length is 348 ft, and the distance between neighboring fractures is 75 ft (shown in Fig. 9). By changing the fracture aperture along the length, two subcases were investigated. In the first subcase (Case 1a), we assume the fractures have a constant aperture of 0.015 feet and a constant permeability of 10,000 md, which gives a high fracture-conductivity of 150 md-ft. In this case, the fractures behave similarly as fractures with infinite conductivity. In the second subcase (Case 2b), we assume the fracture aperture has a linear relationship with the distance x from the wellbore, and fracture permeability is proportional to the square of fracture aperture:

$$w_f(x) = w_{f,\max} \times \left(1 - \frac{x}{x_f}\right), \dots \dots \dots (19)$$

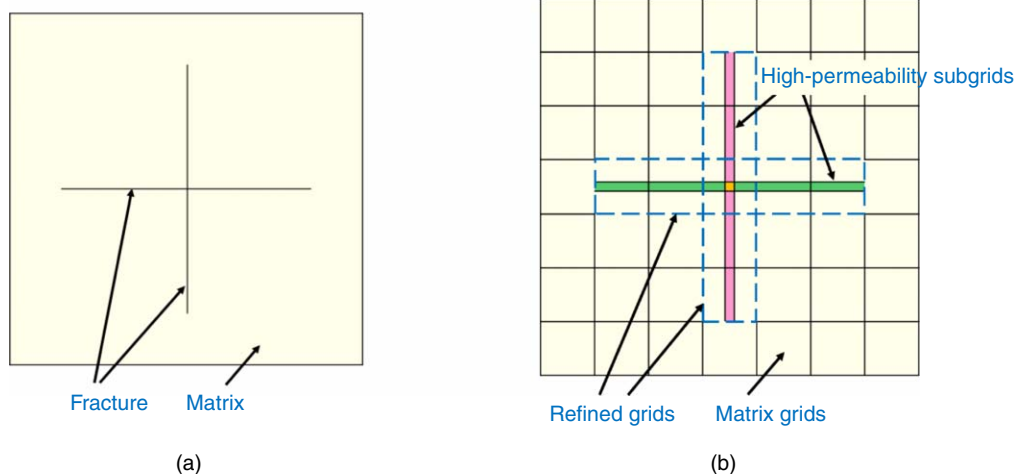


Fig. 8—An example to illustrate the LGR model used in this study. The two intersecting fractures in (a) are represented by high-permeability subgrids in (b). In (b), the purple and green cells are assigned high permeability (the same as the corresponding fractures) and high porosity (1.0). The orange block represents the fracture intersection, and this block has a very small volume.

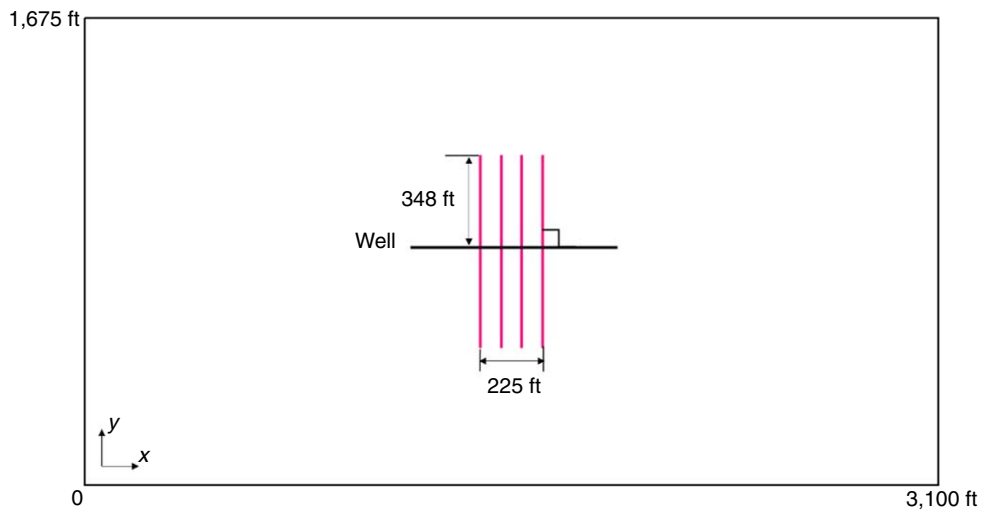


Fig. 9—Reservoir dimensions and transverse hydraulic fractures in Case 1. The purple lines represent the fractures.

$$k_f(x) = k_{f,\max} \times \frac{w_f^2(x)}{w_{f,\max}^2}, \dots \dots \dots (20)$$

where x_f is fracture half-length, $w_{f,\max}$ is the maximum fracture aperture, and $k_{f,\max}$ is the maximum fracture permeability. In Case 2b, we set $w_{f,\max}$ and $k_{f,\max}$ to 0.015 ft and 100 md, respectively. We created an LGR model to approximately simulate the fractures in Case 2b, and each fracture is represented by 49 segments with different fracture apertures and permeabilities. While, in the EDFM, each fracture is discretized into 7 segments, as shown in Fig. 10. The average aperture and effective permeability of each segment are calculated with Eq. 10 and Eq. 16, respectively.

Fig. 11 represents the pressure profiles after one year of production. As we can see, the results are quite similar with negligible difference. Fig. 12 shows a good agreement of gas-flow rate between the two models. This case study tests the Type I and Type II NNCs and shows that the EDFM gives consistent results with the LGR model for bi-wing fracture geometry.

Case 2: Complex Orthogonal Fractures. The operation of hydraulic fracturing may cause the reopening of pre-existing natural fractures, leading to a complex fracture-network. In this case, we show an example involving intersecting orthogonal fractures. All fractures are aligned with one of the axes of the simulation grid; hence, the LGR model can give accurate solution. The reservoir dimension is the same as the previous case. The shape of the hydraulic fractures is the same as in Case 1, and 12 natural fractures are added into the reservoir to form fracture network, as shown in

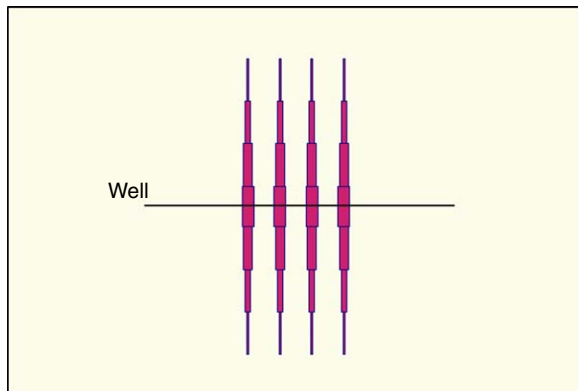


Fig. 10—Hydraulic fractures with variable aperture in Case 1b. The fracture aperture is shown 2,000 times the real size.

Fig. 13. By changing the conductivity of natural fractures, two subcases were investigated. In the first subcase (Case 2a), the natural fractures have the same aperture and permeability as hydraulic fractures. In the second subcase (Case 2b), the permeability of all natural fractures is reduced to 5 md so that they have finite conductivity. To capture the fracture intersection in LGR model, the grids with fracture intersections are refined in the x - and y -direction (3×3). This introduces a small control-volume at each fracture intersection.

Fig. 14 shows the similar pressure profile of LGR model and the EDFM after 240 days of production for Case 2a. The slight pressure difference near the fractures is caused by simplification of transmissibility calculation in the EDFM. Fig. 15 shows a good agreement between gas-flow rate of these models for Cases 2a and 2b. The EDFM accurately handled the fracture intersections with finite fracture-conductivity, illustrating that the EDFM has the capability of modeling fracture network.

Case 3: Nonorthogonal Fractures. During hydraulic fracturing, the fractures tend to grow in the direction perpendicular to the minimum horizontal stress. In some cases, when the well axis deviates from the direction of the minimum horizontal stress, the preferred direction of fracture propagation will not be perpendicular to the wellbore. This often leads to the propagation of nonorthogonal fractures. One of the advantages of the EDFM is its flexibility in modeling nonorthogonal fractures in any orientation.

We present an example in which the fractures have an angle of 63° with the wellbore, as shown in Fig. 16. The fracture aperture and permeability are the same as Case 1. A “zigzag” LGR model with grid size of 1.5×1.5 ft was created in an attempt to approximately represent the nonorthogonal fractures, as shown in Fig. 17, because it is always difficult to “exactly” model a nonorthogonal fracture by grid refinement. The reservoir dimensions were decreased ($523.5 \times 600 \times 80$ ft) compared with previous cases to reduce the simulation time.

The pressure profiles of both LGR model and EDFM are shown in Fig. 18, and the gas-flow-rate curves are presented in Fig. 19, where the close agreement demonstrates the accuracy of the EDFM in modeling nonorthogonal fractures. With the EDFM, we avoid using unstructured grids, and we empower a commercial simulator to model nonorthogonal fractures accurately and effectively without having access to the source code of the simulator.

Case 4: Nonplanar Fractures. The propagation of fractures can also be controlled by several other mechanisms. One of them is the stress interaction between growing fractures, which is commonly referred to as the “stress-shadow” effect. Because of the effect, the fractures in a single fracturing stage may have different

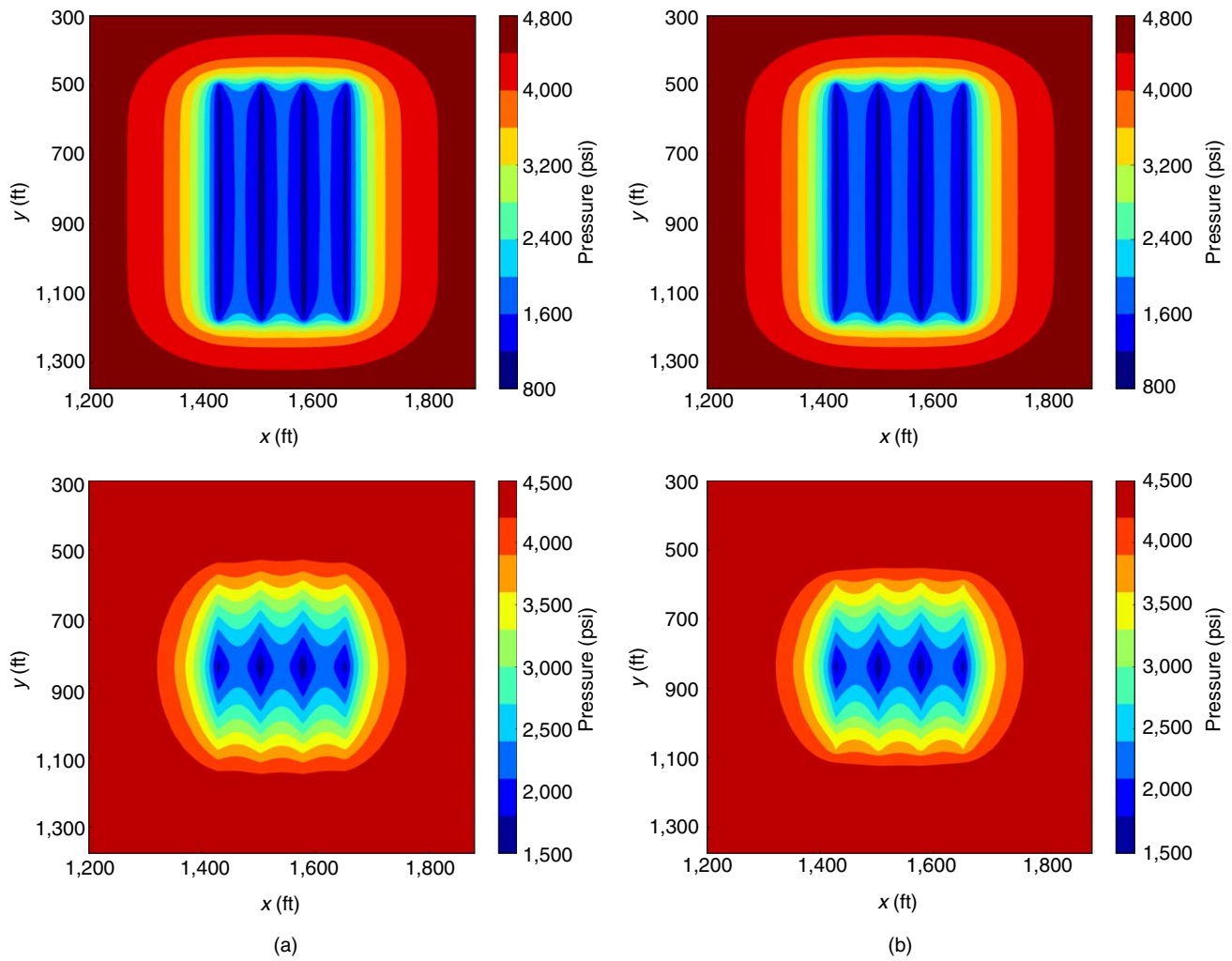


Fig. 11—Pressure profiles (1 year) for Case 1a (top) and Case 1b (bottom) predicted by (a) LGR model and (b) EDFM.

length, resulting in nonplanar fracture shape. Here, we present an example in which the fractures are nonplanar and the fracture length differs in a single fracturing stage. An LGR model was built through the “zigzag” approximation similar to Case 3. Every nonplanar fracture was discretized into two nonorthogonal planar fractures. These two connecting fractures behave as a single nonplanar fracture, as illustrated in previous section. Six small frac-

ture segments were removed with Eq. 18 because of their extra-small control-volume.

The pressure profiles are shown in **Fig. 20**, and the gas-flow-rate curves are presented in **Fig. 21**, where a good agreement demonstrates the accuracy of the EDFM in modeling nonorthogonal fractures. The EDFM can make a general simulator model nonplanar fractures accurately and effectively.

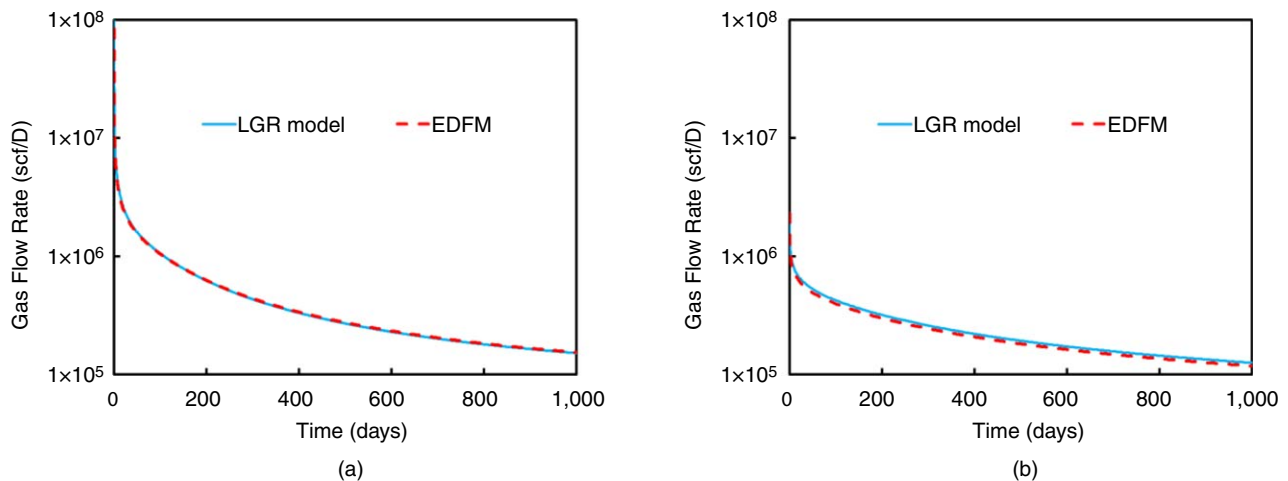


Fig. 12—Gas-flow rate for (a) Case 1a and (b) Case 1b predicted by LGR model and EDFM.

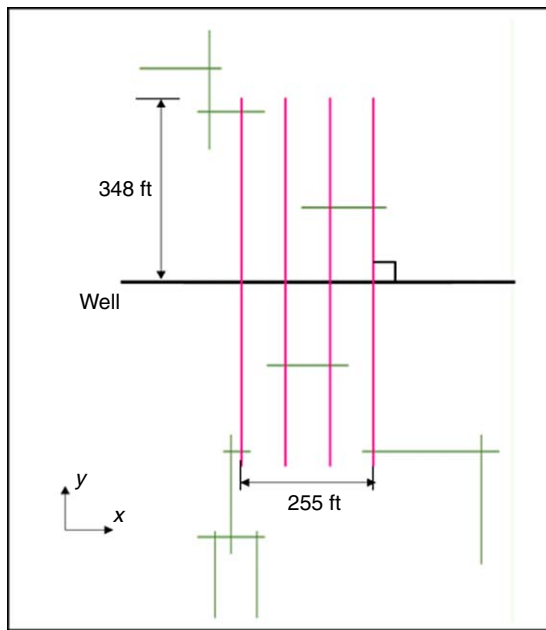


Fig. 13—Fracture network of Case 2. The purple lines represent the hydraulic fractures, and the green lines represent the natural fractures.

Case 5: Complex Nonplanar Fractures With Variable Aperture.

The EDFM has shown its applicability and accuracy compared with LGR models in the previous case studies. When the fractures are highly nonplanar and have variable aperture along the length, the LGR model is not able to handle this case. However, the “embedded” nature of the EDFM gives it the flexibility to model these fractures.

Here, we present a case with hydraulic fractures generated by a fracture-propagation model (Wu and Olson 2014), as shown in Fig. 22. The model provided the fracture aperture at the end of each segment, and we calculated the average aperture and effective permeability with Eq. 10 and Eq. 16 for each segment, respectively. We modeled each nonplanar fracture with 10 interconnected planar fractures. The permeability of the fracture was calculated by the cubic law assuming smooth surface. The reservoir dimensions and grid size are the same as those in Case 1. A semianalytical model is used as a reference solution.

Fig. 23 shows the gas-flow rate for both models, and Fig. 24 gives the pressure profiles at 120 days. As we expected, the EDFM successfully modeled the shape of the complex nonplanar fractures and reached a good agreement with the semianalytical model in gas-flow rate.

CPU-Time Comparison

Computational efficiency is an important factor determining the applicability of a model. Table 2 summarizes the comparison of

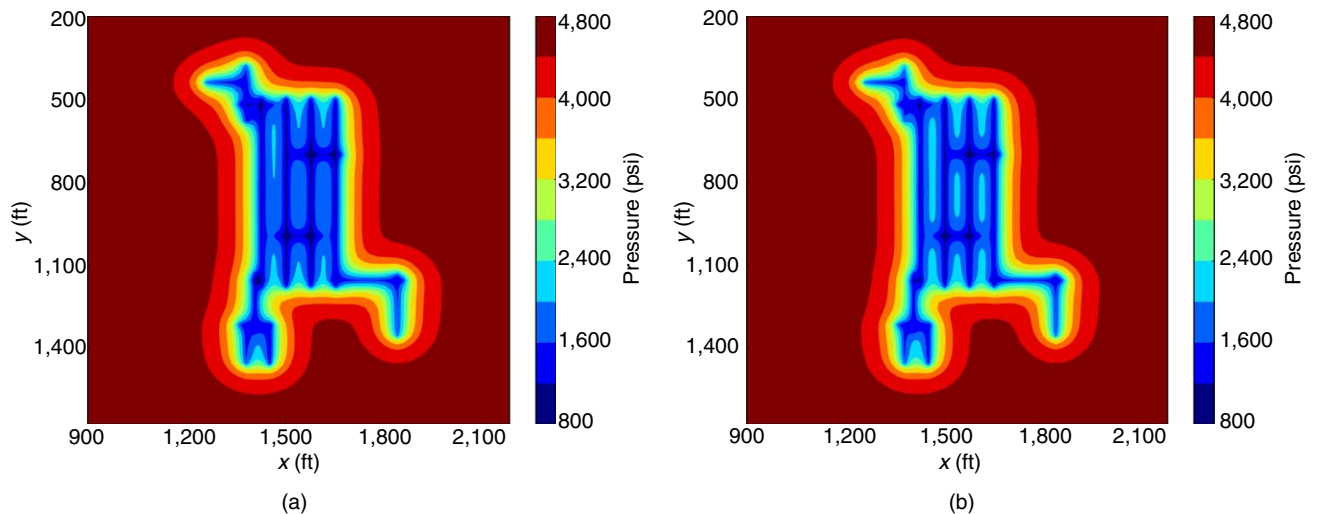


Fig. 14—Pressure profiles (240 days) for Case 2a predicted by (a) LGR model and (b) EDFM.

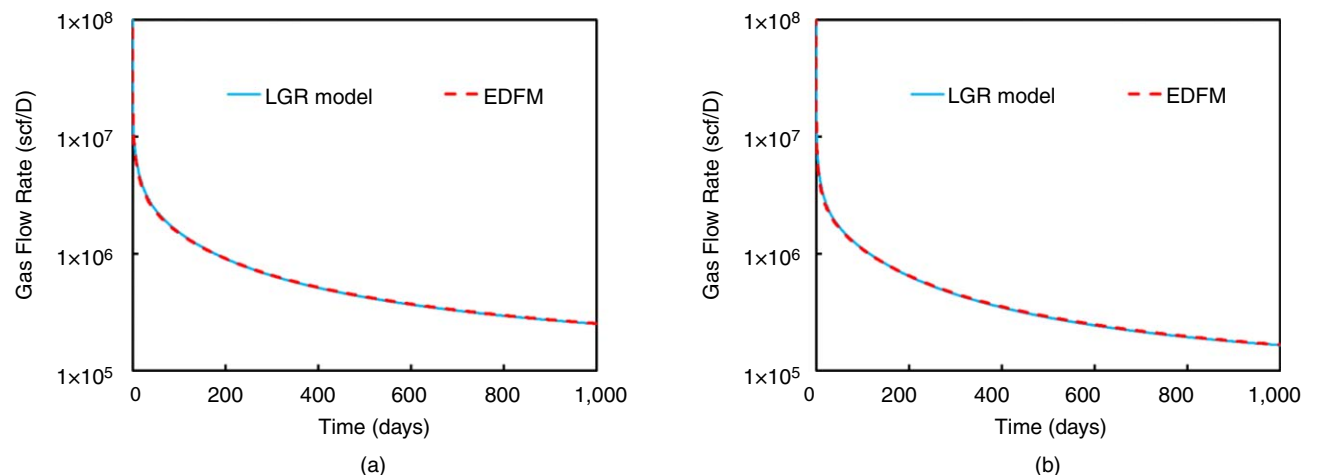


Fig. 15—Gas-flow rate for (a) Case 2a and (b) Case 2b predicted by LGR model and EDFM.

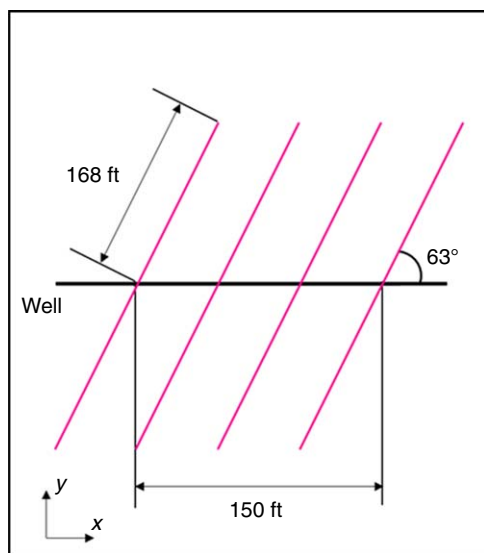


Fig. 16—Nonorthogonal fractures in Case 3. The purple lines represent the hydraulic fractures.

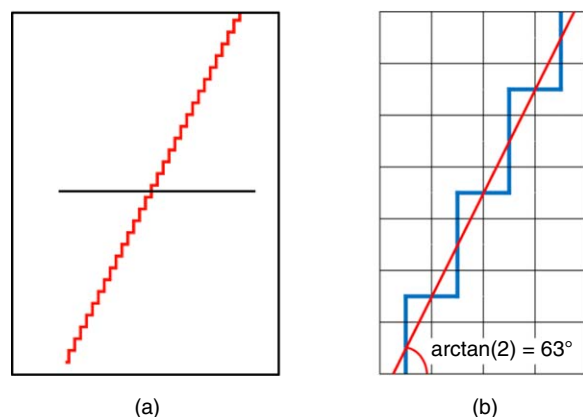


Fig. 17—Explanation of “zigzag” in Case 3. The red lines in (a) represent the high-permeability subgrids for fractures. A closer view is given in (b), where the red line shows the actual fracture shape, and the blue lines show the “zigzag” representation of the fracture shape.

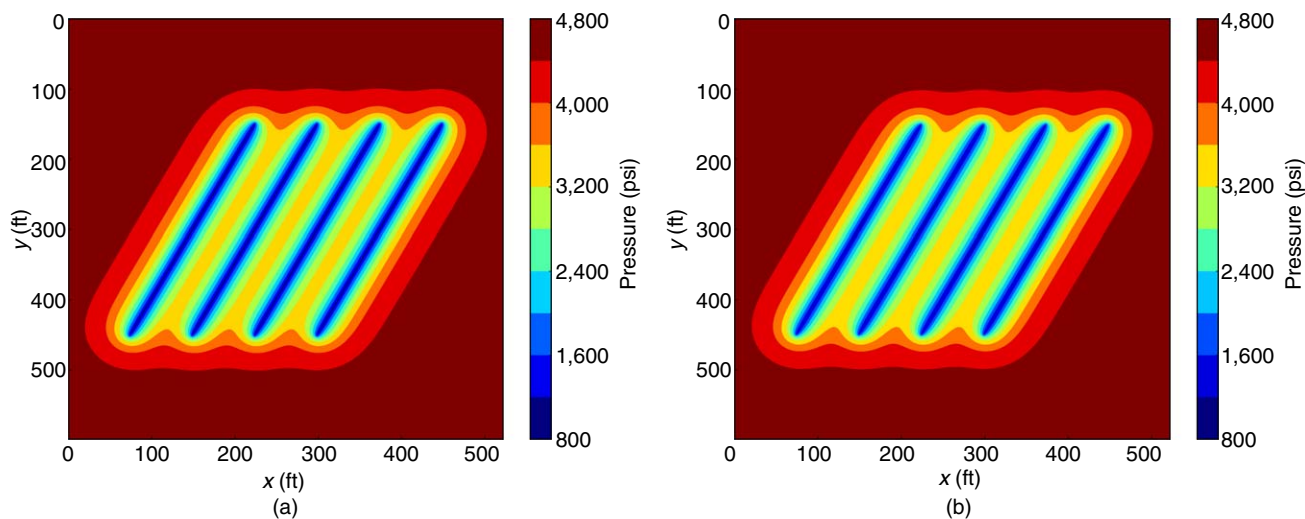


Fig. 18—Pressure profiles (60 days) for Case 3 predicted by (a) LGR model and (b) EDFM.

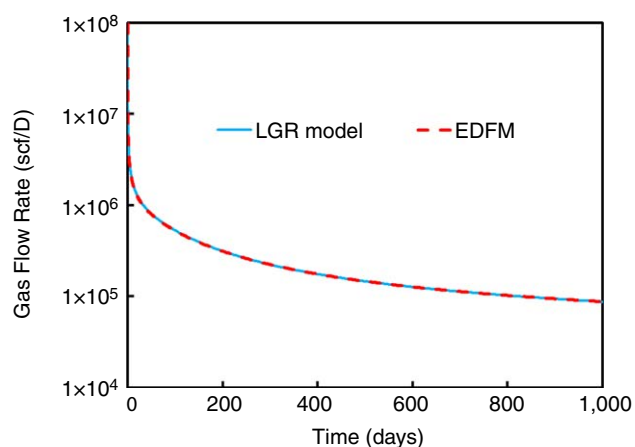


Fig. 19—Gas-flow rate for nonorthogonal fracture (Case 3) predicted by LGR model and EDFM.

central processing unit (CPU) time between EDFM and LGR models for RS1.

In Table 2, T_{total} is the CPU time for a case with LGR model or EDFM. T_{nofrac} is the CPU time for the same case without fractures. $T_{\text{EDFM}}/T_{\text{LGR}}$ is the CPU time ratio of the EDFM to LGR model. N_m is the total number of matrix cells. N_{extra} is the extra number of grids introduced by EDFM or LGR (in the LGR models).

As we can see, although N_{extra} is much smaller than N_m , there is always a large increase in CPU time after introducing these extra grids. Therefore, these extra cells play an important role in limiting the CPU efficiency. For orthogonal cases (Case 1 and Case 2), the fractures can be precisely modeled by LGR, but the number of extra cells in LGR model is higher than that in EDFM. In Cases 1a and 1b, EDFM has no advantage over LGR model. However, as the number of extra cells increases, the EDFM has better performance than the LGR models in Cases 2a and 2b.

For nonorthogonal or nonplanar fracture cases (Case 3 and Case 4), to approximate the incline angle, the LGR model requires many more extra cells because of grid refinement. In addition, for

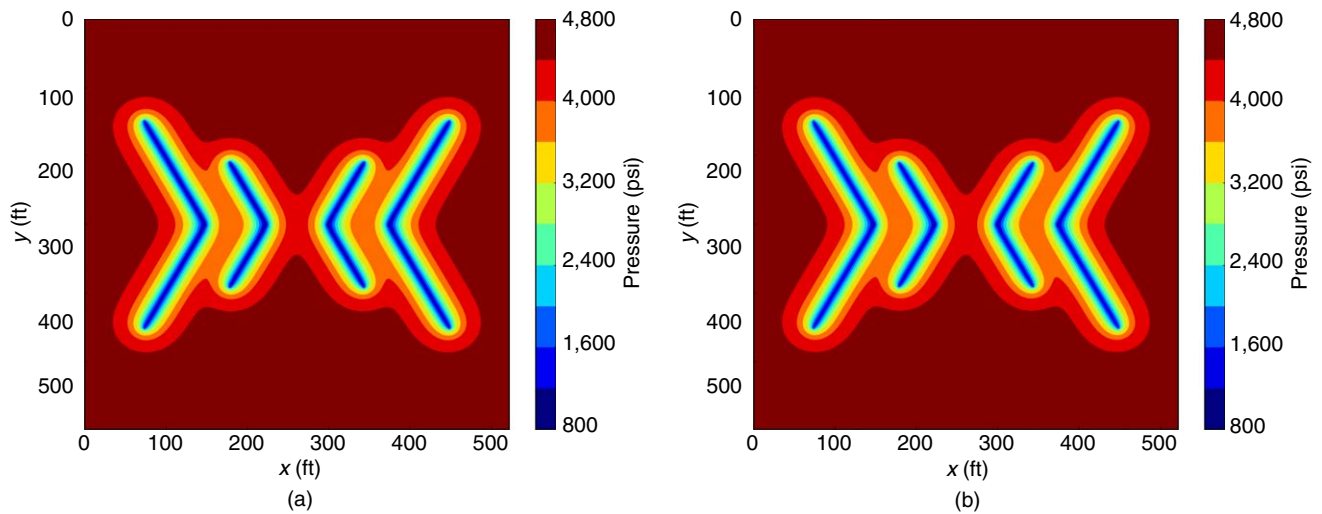


Fig. 20—Pressure profiles (30 days) for Case 4 predicted by (a) LGR model and (b) EDFM.

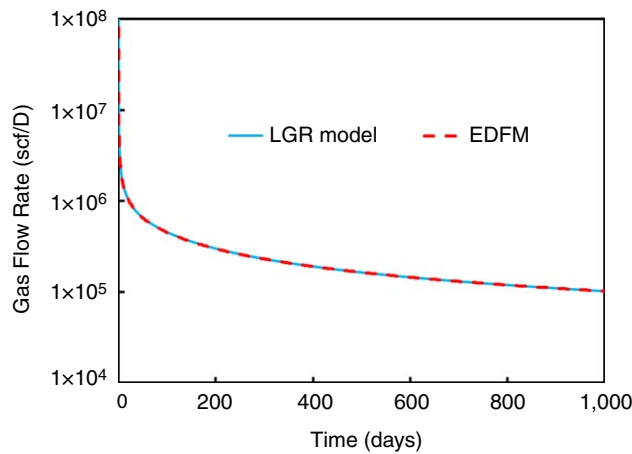


Fig. 21—Gas-flow rate for simple nonplanar fracture (Case 4) predicted by LGR model and EDFM.

LGR models, the small control-volumes at fracture intersections undermine the simulation timestep. As a result, the EDFM has a great advantage over LGR models regarding CPU performance. Furthermore, the EDFM is flexible in modeling irregular fracture-shapes, which is challenging for the LGR model.

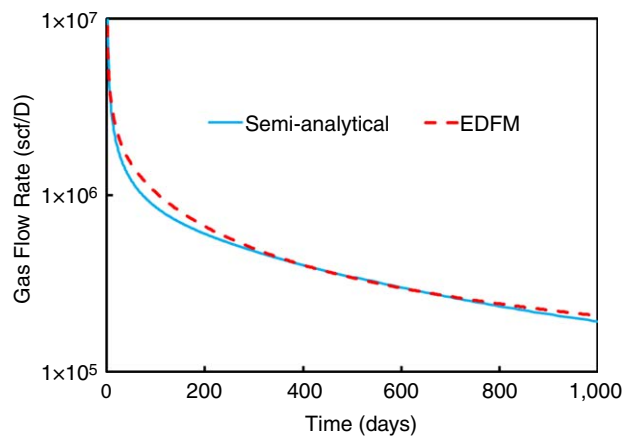


Fig. 23—Gas-flow rate for nonplanar fractures with variable aperture (Case 5) predicted by EDFM and semianalytical model.

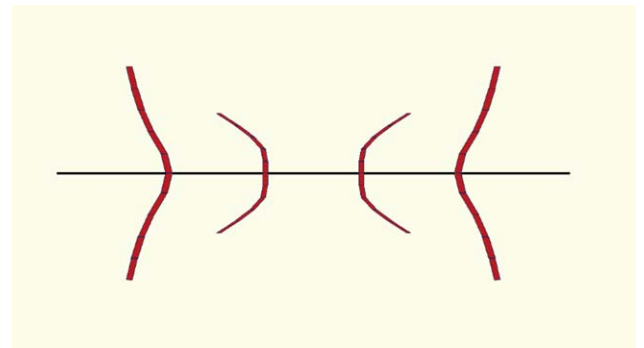


Fig. 22—Hydraulic-fracture well shape for Case 5. The length in y-direction is shown 0.2 times the real size to clearly show the nonplanar shape. The fracture aperture is shown 1,000 times the real size.

The comparison clearly illustrates the difference between the EDFM and the LGR model. For the LGR model, many extra cells are required around the fractures to model the complex fracture-shape, leading to a high computational cost. However, the EDFM avoids this problem by handling the connections mathematically without losing accuracy.

Because we performed all the case studies with both RS1 and RS2, the CPU time of EDFM for all cases in RS1 and RS2 is summarized in **Table 3**. In both simulators, the EDFM shows a high computational performance. **Table 4** shows the difference in cumulative gas production at 1,000 days between RS1 and RS2. It can be observed that high consistency was obtained between both simulators.

It should be noted that the EDFM introduces off-diagonal terms in the discretized pressure matrix, and this may lead to more solver iterations in the computations. Therefore, the computational speed of the EDFM can be affected by the performance of the linear solver used in the simulators. For example, In RS2, we observed a great difference in CPU performance for different solvers. For cases with nonorthogonal fractures, the constrained pressure residual preconditioner has a better performance than the nested factorization preconditioner. We recommend this preconditioner for EDFM simulations because of its efficient reordering of the operating matrix.

The case studies in our paper show the high computational efficiency of the EDFM in the two reservoir simulators used in this work. Although the performance of the EDFM may vary in different simulators, we expect the EDFM to be faster than LGR model for complex fracture geometries.

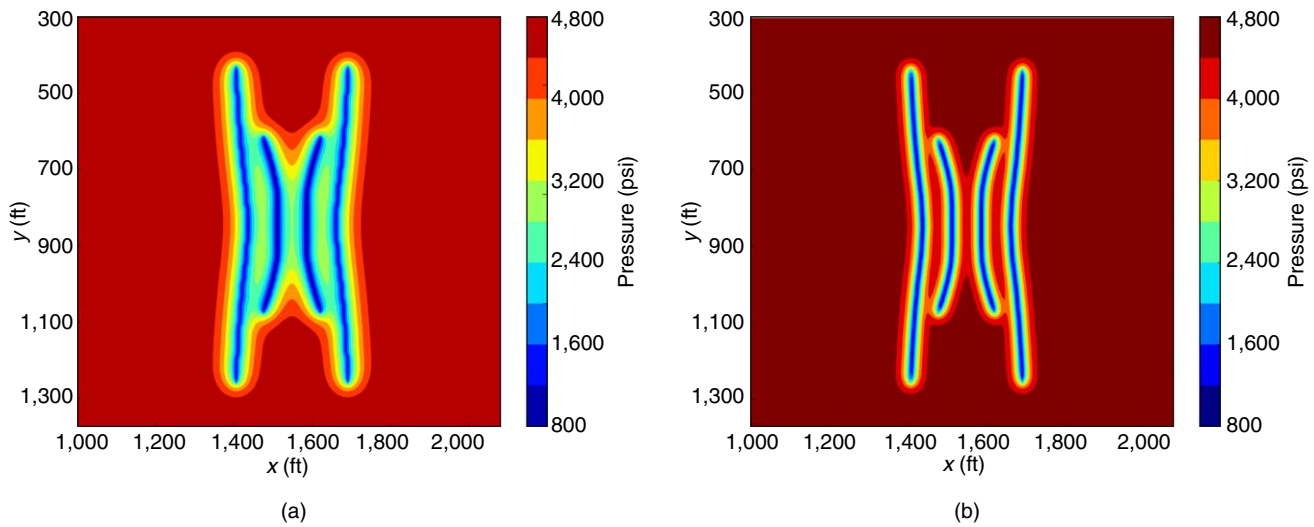


Fig. 24—Pressure profiles (120 days) for Case 5 predicted by (a) EDFM and (b) semianalytical model.

Case	Model	T_{total} (seconds)	T_{nofrac} (seconds)	$T_{\text{EDFM}}/T_{\text{LGR}}$	N_m	N_{extra}	Number of Newton Cycles	
Case 1a	LGR	18	7	1.28	19,800	392	141	
	EDFM	23				196	210	
Case 1b	LGR	17		1.09		392	138	
	EDFM	19				196	137	
Case 2a	LGR	52		0.87		802	328	
	EDFM	45				373	320	
Case 2b	LGR	34		0.91		802	269	
	EDFM	31				373	218	
Case 3	LGR	7,676	46	0.05	139,600	9,696	2,253	
	EDFM	361				1,204	332	
Case 4	LGR	8,814		0.05		7,776	2,032	
	EDFM	466				984	383	

Table 2—CPU time comparison between LGR models and EDFM for different cases in RS1.

Case	Case 1a	Case 1b	Case 2a	Case 2b	Case 3	Case 4	Case 5	Case 6a	Case 6d	Case 7
T_{total} of RS1 (seconds)	23	19	45	31	361	466	41	60	102	3995
T_{total} of RS2 (seconds)	7	4	5	4	64	40	4	18	20	2921

Table 3—CPU time of the EDFM for different cases for both RS1 and RS2.

Case	Case 1a	Case 1b	Case 2a	Case 2b	Case 3	Case 4	Case 5	Case 6a	Case 6d
Error	0.30%	0.19%	0.84%	1.61%	0.39%	0.86%	1.75%	0.31%	1.01%

Table 4—Difference in cumulative gas production at 1,000 days between RS1 (EDFM) and RS2 (EDFM).

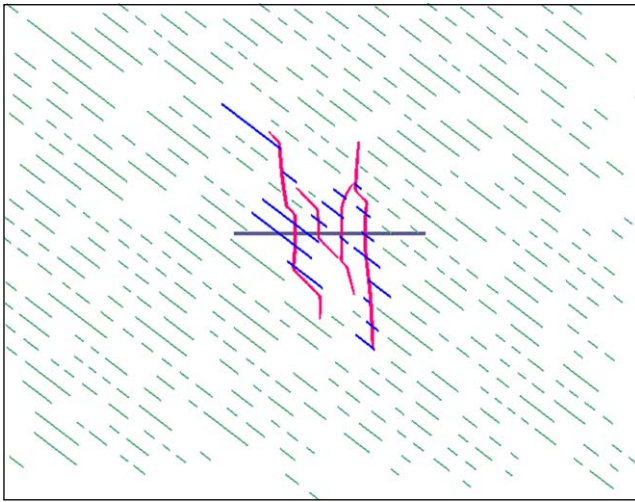


Fig. 25—Hydraulic fracture (purple) and natural fracture wells (green and blue) for Case 6. The aperture of hydraulic fractures is shown 1,000 times the real size. The blue lines represent the natural fractures that intersect the hydraulic fractures, and the green lines represent the “disconnected” natural fractures. The number of “blue” fractures is 17, and the number of “green” fractures is 360.

Model Application

In the previous sections, the EDFM was shown to be a powerful extension of conventional reservoir simulators to handle shale reservoirs with complex fracture geometries. It is applicable to naturally fractured reservoirs as well as hydraulically fractured reservoirs (Moinfar et al. 2014; Cavalcante Filho et al. 2015). In this section, we present two case studies of the EDFM in shale reservoirs with nonplanar hydraulic fractures and inclusion of many natural fractures.

Case 6: Shale Gas Production in a Naturally Fractured Reservoir. The same grids and reservoir parameters as in Case 1 are used in this study. The hydraulic fractures and natural fractures are shown in Fig. 25. Each nonplanar hydraulic fracture is discretized into 75 planar fractures with different apertures, and each natural fracture is represented by a single fracture plane. The pre-existing natural fractures have a dominant direction, as shown in the figure. The natural-fracture conductivity is assumed to be 1 md-ft in this study. Some natural fractures near the wellbore affected the propagation of hydraulic fractures by diverting their growth path. All natural fractures are divided into two groups, as shown in different colors in Fig. 25. The blue lines represent the natural fractures that intersect the hydraulic fractures. They become part of the fracture network and increase the contact area between hydraulic fractures and the reservoir. The green lines represent other natural fractures, which are disconnected and relatively far from the well. The intersections between wellbore and natural fractures are not considered in this study.

Four comparative simulation runs were performed to investigate how these two groups of fractures affect the well performance separately. In Case 6a, only the hydraulic fractures are considered. In Cases 6b and 6c, in addition to the hydraulic fractures, the natural fractures, “green” and “blue,” are added into the reservoir, respectively. In Case 6d, all the hydraulic and natural fractures are modeled in the simulation.

The influence of different kinds of natural fractures on production is shown in Fig. 26. An observation is that the gas production of Cases 6a and 6b is much higher than that of Cases 6c and 6d, indicating the large influence of the connected “blue” fractures. In addition, in early time (before 200 days), the cumulative production curve of Cases 6a and 6b almost overlap, and the gas production of Case 6c is almost the same as that of Case 6d. This indicates that the “green” fractures are not evidently influencing the early-time production. In late time (after 200 days), the

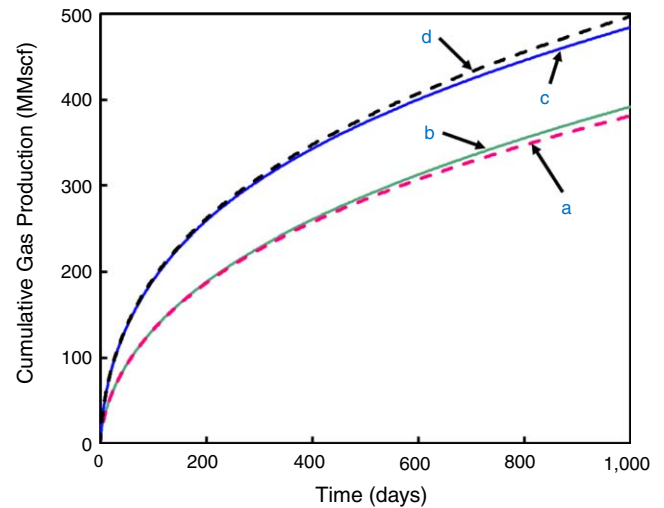


Fig. 26—Cumulative gas production for Case 6.

“green” fractures began to affect the production because the gas rate of Case 6b is evidently higher than Case 6a. The reason is that those “green” fractures enhance the flow in the region far from the wellbore and decrease the time for gas to reach the fracture network.

The pressure profiles shown in Fig. 27 further illustrate the impact of the fractures. The influence of the “green” natural fractures can be easily observed in Fig. 27. Although they are not as highly conductive as hydraulic fractures, their influence on the pressure distribution around the fractures cannot be ignored. In contrast, the “blue” natural fractures are not obviously affecting the pressure field around the hydraulic fractures because they are implicitly enhancing the overall matrix permeability.

This example shows the influences of different types of natural fractures on production. The connectivity between natural fractures with hydraulic fractures can greatly influence both the early-time and late-time production and the existence of a large number of natural fractures affect the late-time production significantly. For prediction of only early-time production, it is possible to ignore the “disconnected” natural fractures.

It is also shown in this case that the EDFM can effectively model the fracture network and disconnected natural fractures. It provides a powerful tool in rapid production analysis for highly fractured reservoirs.

Case 7: A 3D, Three-Phase, Multicomponent Simulation. As we mentioned previously, the EDFM can be used as a general procedure in both 2D and 3D cases, and for both compositional and black-oil formulations. In real field applications, compositional simulations are often used. In addition, the reservoir may have multiple layers, and the height of the hydraulic fractures can be smaller than reservoir height. Therefore, we present a 3D, compositional simulation example to show the application of the EDFM in a typical field study.

The reservoir dimensions are $6,000 \times 1,500 \times 80$ ft and a uniform $300 \times 75 \times 5$ matrix grid is used in this study. The reservoir parameters are shown in Table 5. The fluid properties of the Bakken formation are used in the simulation by assuming seven pseudocomponents: CO_2 , N_2 , CH_4 , $\text{C}_2\text{--C}_4$, $\text{C}_5\text{--C}_7$, $\text{C}_8\text{--C}_9$, and C_{10+} , and their molar fractions: 0.02, 0.04, 25, 22, 20, 13, and 19.94%, respectively. More details of the fluid properties can be found in Yu et al. (2015). The Peng-Robinson equation of state (Peng and Robinson 1976) is used here to calculate the hydrocarbon-phase behavior. The capillary effect is not considered in this study. For matrix gridblocks, a Corey-type relative permeability curve is used for water and gas, and corresponding parameters are also shown in Table 6. Stone’s second model is used for three-phase oil relative permeability. For fracture cells, a straight-line relative permeability model is used for all phases.

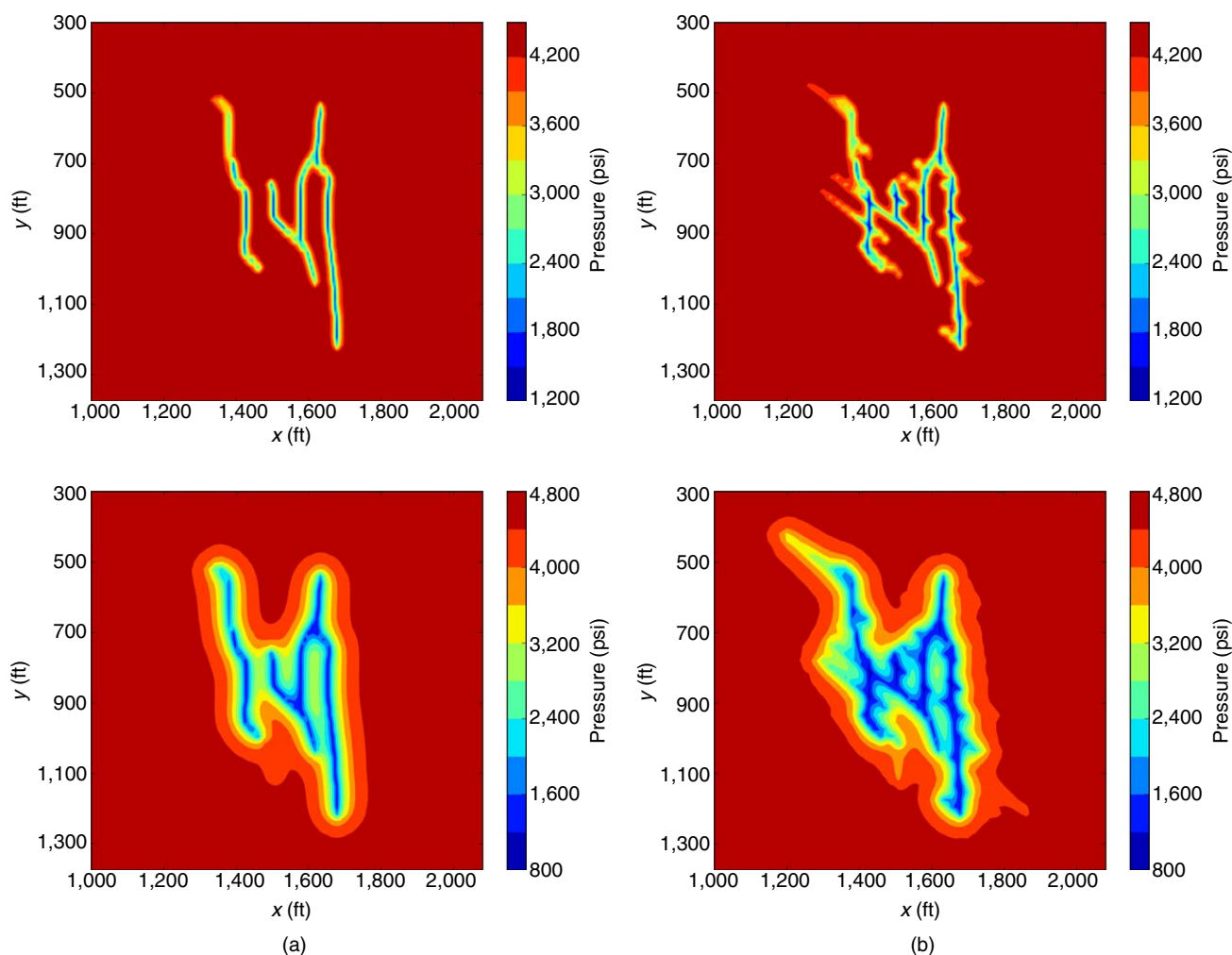


Fig. 27—Pressure profiles (10 days and 105 days) for (a) Case 6a (no natural fracture) and (b) Case 6d (with all natural fractures).

Parameter	Value	Unit
Reservoir permeability	0.002	md
Reservoir porosity	7%	—
Initial reservoir pressure	2,000	psi
Reservoir thickness	80	ft
Rock compressibility	1×10^{-6}	psi ⁻¹
Depth of top layer	1,000	ft
Initial water saturation	40%	—
Water viscosity	0.243	cp
Water density	62.8	lbm/ft ³
Reservoir temperature	240	°F
Wellbore radius	0.25	ft
Bottomhole pressure	500	psi
Simulation time	1,000	days

Table 5—Basic reservoir and operation parameters in simulation for Case 7.

Fifteen hydraulic fractures and 200 natural fractures are put in to the reservoir (as shown in Fig. 28). Each hydraulic fracture is discretized into 11 segments with the fracture width ranging from 0.001 to 0.015 ft. The fracture permeability is constant (10,000 md). The conductivity of natural fractures is 1 md-ft. All natural fractures fully penetrate the reservoir height, with dip angles ranging from 60 to 90°. The hydraulic fractures partially penetrate the

Parameter	Value
Residual water saturation	20%
Residual oil saturation	10%
Residual gas saturation	10%
Water relative permeability endpoint	0.7
Oil relative permeability endpoint	0.8
Gas relative permeability endpoint	0.8
Water relative permeability exponent	2.0
Oil relative permeability exponent	2.0
Gas relative permeability exponent	2.0

Table 6—Parameters for matrix relative permeability curve for Case 7.

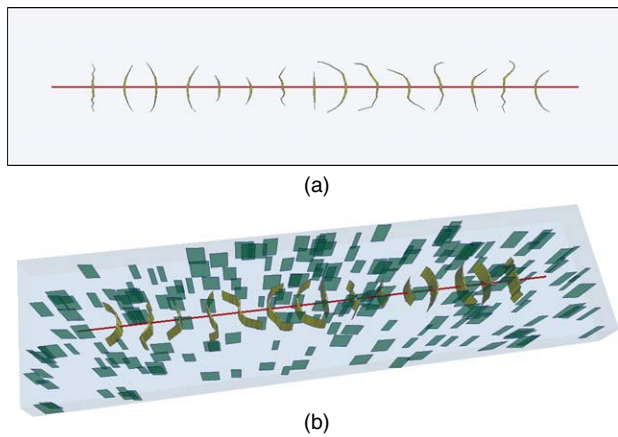


Fig. 28—Reservoir dimensions and fractures in Case 7. The yellow planes represent hydraulic fractures, and the green planes represent natural fractures. (a) Top view of hydraulic fractures. The fracture apertures are shown 1,000 times the real size. (b) 3D view of hydraulic fractures and natural fractures.

reservoir in vertical direction, with a distance of 16 ft from the top and bottom of the reservoir, respectively.

Fig. 29 shows the water, oil, and gas production predicted by the EDFM. **Fig. 30** shows the profiles of pressure, mole fraction of C_8-C_9 in oleic phase, and gas saturation after 1,000 days of production calculated by the EDFM. Some hydraulic fractures are connected by natural fractures. The pressure profile indicates the

pressure interference between neighboring hydraulic fractures, which is greatly influenced by fracture geometry. By use of the compositional model in RS1 and RS2, the CPU times for Case 7 without fractures are 956 seconds and 549 seconds, respectively. After adding fractures with the EDFM, the CPU times are 3,995 seconds (in RS1) and 2,921 seconds (in RS2).

Conclusions

The procedure presented in this paper can be applied in a noninvasive way in traditional reservoir simulators with NNC functionality. The EDFM keeps the structured grids of conventional simulators, and models the fractures implicitly through different types of connection factors. Assumptions and limitations of the EDFM formulations were also discussed.

Nonplanar fractures and fractures with variable aperture can be appropriately modeled through fracture intersection and effective aperture, respectively. A technique to remove very-small fracture segments in the EDFM was proposed. The accuracy of the EDFM was confirmed by comparison with the LGR model and a semianalytical solution. Comparison of the computational time showed the advantage of the EDFM over the LGR model. The EDFM is flexible in handling fractures with complex geometry without introducing a large number of extra cells, which guarantees its computational efficiency.

The case study showed the applicability of the EDFM in hydraulically fractured reservoirs with a fracture network and a large number of natural fractures. The influence of different types of natural fractures can be modeled appropriately by the EDFM. The 3D, multiphase, multicomponent simulation example demonstrates the potential application of the EDFM in real field studies.

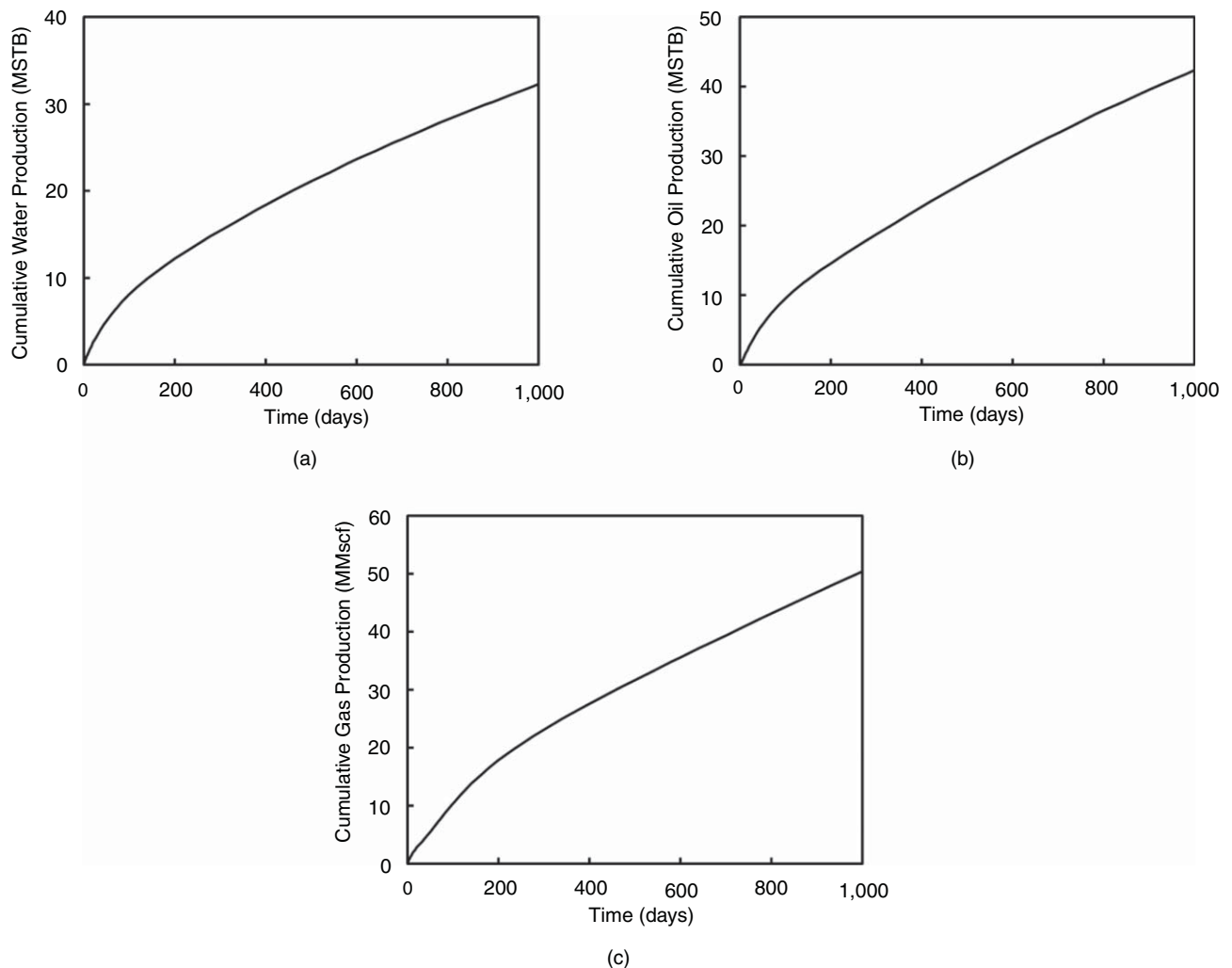


Fig. 29—Cumulative production predicted by the EDFM for (a) water, (b) oil, and (c) gas.

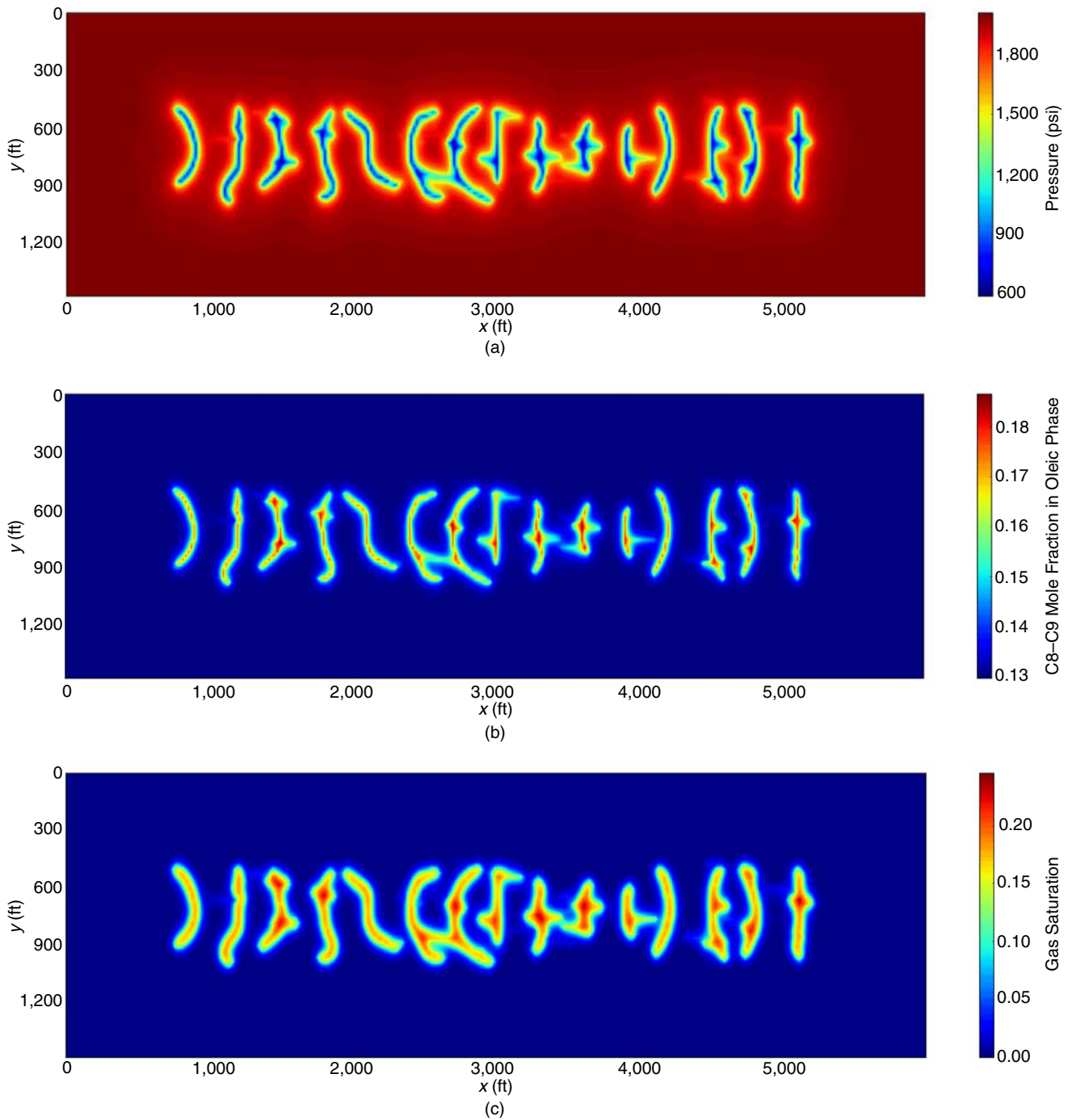


Fig. 30—Profiles of (a) pressure, (b) C₈–C₉ mole fraction in the oleic phase, and (c) gas saturation after 1,000 days of production predicted by the EDFM (Layer 3).

Nomenclature

A = area, ft
 B = formation volume factor (FVF)
 c = compressibility, psi^{-1}
 C_f = fracture conductivity, md-ft
 \bar{d} = average distance, ft
 dS = area element, ft^2
 dV = volume element, ft^3
 H = fracture height, ft
 H_s = height of fracture segment, ft
 k = reservoir permeability, md
 k_f = fracture permeability, md
 k_{α} = differential equilibrium-portioning coefficient of gas at a constant temperature
 K = matrix-permeability tensor, md
 L = fracture length, ft

L_{int} = length of fracture-intersection line, ft
 L_s = length of fracture segment, ft
 \vec{n} = normal vector
 N = number of NNCs
 p = pressure, psi
 Q = volume flow rate, ft^3/D
 re = effective radius, ft
 rw = wellbore radius, ft
 R_s = solution-gas-oil ratio, scf/STB
 S = fracture-segment area, ft^2
 T = transmissibility factor, md-ft
 T_R = reservoir temperature, $^{\circ}\text{F}$
 V = volume, ft^3
 V_b = bulk volume, ft^3
 V_m = Langmuir isotherm constant, scf/ton
 w_f = fracture aperture, ft

\bar{w}_f = average fracture aperture, ft
 w_I = well index, md-ft
 x = distance, ft
 x_f = fracture half-length, ft
 Δp = pressure drop, psi
 λ = phase mobility, cp^{-1}
 μ = viscosity, cp
 ρ = density, g/cm^3
 ϕ_f = fracture-effective porosity

Subscripts and Superscripts

a = adsorbed
 b = bulk
 c = common face
 eff = effective
 f = fracture
 g = gas
 int = fracture intersection
 j = phase
 L = Langmuir
 m = matrix
 o = oil
 seg = fracture segment
 ST = stock tank

Acknowledgments

We would like to acknowledge Statoil and the sponsors of the Reservoir Simulation Joint Industry Project at the Center for Petroleum and Geosystems Engineering at the University of Texas at Austin for supporting this work. We would also like to acknowledge Kan Wu and Jon Olson for providing complex nonplanar fracture-geometry case studies with their fracture-propagation model, which was supported by the Fracture Research and Application Consortium at the University of Texas at Austin.

References

- Abass, H. H., Hedayati, S., and Meadows, D. L. 1996. Nonplanar Fracture Propagation From a Horizontal Wellbore: Experimental Study. *SPE Prod & Fac* **11** (3): 133–137. SPE-24823-PA. <http://dx.doi.org/10.2118/24823-PA>.
- Al-Hinai, O., Singh, G., Pencheva, G. et al. 2013. Modeling Multiphase Flow With Nonplanar Fractures. Presented at the SPE Reservoir Simulation Symposium, The Woodlands, Texas, 18–20 February. SPE-163605-MS. <http://dx.doi.org/10.2118/163605-MS>.
- Berkowitz, B., Naumann, C., and Smith, L. 1994. Mass Transfer at Fracture Intersections: An Evaluation of Mixing Models. *Water Resour. Res.* **30** (6): 1765–1773. <http://dx.doi.org/10.1029/94WR00432>.
- Cavalcante Filho, J. S. A., Shakiba, M., Moinfar, A. et al. 2015. Implementation of a Preprocessor for Embedded Discrete Fracture Modeling in an IMPEC Compositional Reservoir Simulator. Presented at the SPE Reservoir Simulation Symposium, Houston, 23–25 February. SPE-173289-MS. <http://dx.doi.org/10.2118/173289-MS>.
- Cipolla, C. L., Warpinski, N. R., Mayerhofer, M. et al. 2010. The Relationship Between Fracture Complexity, Reservoir Properties, and Fracture-Treatment Design. *SPE Prod & Oper* **25** (4): 438–452. SPE-115769-PA. <http://dx.doi.org/10.2118/115769-PA>.
- El Rabaa, W. 1989. Experimental Study of Hydraulic Fracture Geometry Initiated From Horizontal Wells. Presented at the SPE Annual Technical Conference and Exhibition, San Antonio, Texas, USA, 8–11 October. SPE-19720-MS. <http://dx.doi.org/10.2118/19720-MS>.
- Fisher, M. K., Heinze, J. R., Harris, C. D. et al. 2004. Optimizing Horizontal Completion Techniques in the Barnett Shale Using Microseismic Fracture Mapping. Presented at the SPE Annual Technical Conference and Exhibition, Houston, 26–29 September. SPE-90051-MS. <http://dx.doi.org/10.2118/90051-MS>.
- Gale, J. F. W., Reed, R. M., and Holder, J. 2007. Natural Fractures in the Barnett Shale and Their Importance for Hydraulic Fracture Treatments. *AAPG Bull.* **91** (4): 603–622. <http://dx.doi.org/10.1306/11010606061>.
- Hajibeygi, H., Karvounis, D., and Jenny, P. 2011. A Hierarchical Fracture Model for the Iterative Multiscale Finite Volume Method. *J. Comput. Phys.* **230** (24): 8729–8743. <http://dx.doi.org/10.1016/j.jcp.2011.08.021>.
- Hoteit, H. and Firoozabadi, A. 2006. Compositional Modeling of Discrete-Fractured Media Without Transfer Functions by the Discontinuous Galerkin and Mixed Methods. *SPE J.* **11** (3): 341–352. SPE-90277-PA. <http://dx.doi.org/10.2118/90277-PA>.
- Hui, M.-H., Mallison, B. T., Fyrozjaee, M. H. et al. 2013. The Upscaling of Discrete Fracture Models for Faster, Coarse-Scale Simulations of IOR and EOR Processes for Fractured Reservoirs. Presented at the SPE Annual Technical Conference and Exhibition, New Orleans, 30 September–2 October. SPE-166075-MS. <http://dx.doi.org/10.2118/166075-MS>.
- Jiang, J., Shao, Y., and Younis, R. M. 2014. Development of a Multi-Continuum Multi-Component Model for Enhanced Gas Recovery and CO₂ Storage in Fractured Shale Gas Reservoirs. Presented at the SPE Improved Oil Recovery Symposium, Tulsa, 12–16 April. SPE-169114-MS. <http://dx.doi.org/10.2118/169114-MS>.
- Karimi-Fard, M. and Firoozabadi, A. 2003. Numerical Simulation of Water Injection in Fractured Media Using the Discrete-Fractured Model and the Galerkin Method. *SPE Res Eval & Eng* **6** (2): 117–126. SPE-83633-PA. <http://dx.doi.org/10.2118/83633-PA>.
- Karimi-Fard, M., Durlofsky, L. J., and Aziz, K. 2004. An Efficient Discrete-Fracture Model Applicable for General-Purpose Reservoir Simulators. *SPE J.* **9** (2): 227–236. SPE-88812-PA. <http://dx.doi.org/10.2118/88812-PA>.
- Langmuir, I. 1918. The Adsorption of Gases on Plane Surfaces of Glass, Mica and Platinum. *J. Am. Chem. Soc.* **40**: 1403–1461. <http://dx.doi.org/10.1021/ja02242a004>.
- Lee, S. H., Lough, M. F., and Jensen, C. L. 2001. Hierarchical Modeling of Flow in Naturally Fractured Formations With Multiple Length Scales. *Water Resour. Res.* **37** (3): 443–455. <http://dx.doi.org/10.1029/2000WR900340>.
- Li, L. and Lee, S. H. 2008. Efficient Field-Scale Simulation of Black Oil in a Naturally Fractured Reservoir Through Discrete Fracture Networks and Homogenized Media. *SPE Res Eval & Eng* **11** (4): 750–758. SPE-103901-PA. <http://dx.doi.org/10.2118/103901-PA>.
- Marcondes, F., Varavei, A., and Sepehrnoori, K. 2010. An Element-Based Finite-Volume Method Approach for Naturally Fractured Compositional Reservoir Simulation. Presented at the 13th Brazilian Congress of Thermal Sciences and Engineering—ENCIT, Uberlândia, MG, Brazil, 5–10 December.
- Matthai, S., Menzentsev, A., and Belayneh, M. 2005. Control-Volume Finite-Element Two-Phase Flow Experiments With Fractured Rock Represented by Unstructured 3D Hybrid Meshes. Presented at the SPE Reservoir Simulation Symposium, The Woodlands, Texas, 31 January–2 February. SPE-93341-MS. <http://dx.doi.org/10.2118/93341-MS>.
- Maxwell, S. C., Urbancic, T. I., Steinsberger, N. et al. 2002. Microseismic Imaging of Hydraulic Fracture Complexity in the Barnett Shale. Presented at the SPE Annual Technical Conference and Exhibition, San Antonio, Texas, USA, 29 September–2 October. SPE-77440-MS. <http://dx.doi.org/10.2118/77440-MS>.
- Moinfar, A., Varavei, A., Sepehrnoori, K. et al. 2013. Development of a Coupled Dual Continuum and Discrete Fracture Model for the Simulation of Unconventional Reservoirs. Presented at the SPE Reservoir Simulation Symposium, The Woodlands, Texas, USA, 18–20 February. SPE-163647-MS. <http://dx.doi.org/10.2118/163647-MS>.
- Moinfar, A., Varavei, A., Sepehrnoori, K. et al. 2014. Development of an Efficient Embedded Discrete Fracture Model for 3D Compositional Reservoir Simulation in Fractured Reservoirs. *SPE J.* **19** (2): 289–303. SPE-154246-PA. <http://dx.doi.org/10.2118/154246-PA>.
- Monteagudo, J. and Firoozabadi, A. 2004. Control-Volume Method for Numerical Simulation of Two-Phase Immiscible Flow in Two- and Three-Dimensional Discrete-Fractured Media. *Water Resour. Res.* **40** (7): 1–20. <http://dx.doi.org/10.1029/2003WR002996>.
- Noorishad, J. and Mehran, M. 1982. An Upstream Finite Element Method for Solution of Transient Transport Equation in Fractured Porous Media. *Water Resour. Res.* **18** (3): 588–596. <http://dx.doi.org/10.1029/WR018i003p00588>.
- Olorode, O., Freeman, C. M., Moridis, G. et al. 2013. High-Resolution Numerical Modeling of Complex and Irregular Fracture Patterns in Shale-

- Gas Reservoirs and Tight Gas Reservoirs. *SPE Res Eval & Eng* **16** (4): 443–455. SPE-152482-PA. <http://dx.doi.org/10.2118/152482-PA>.
- Olson, J. E. 2008. Multi-Fracture Propagation Modeling: Applications to Hydraulic Fracturing in Shales and Tight Gas Sands. Presented at the 42nd US Rock Mechanics Symposium (USRMS), San Francisco, 29 June–2 July.
- Panfili, P. and Cominelli, A. 2014. Simulation of Miscible Gas Injection in a Fractured Carbonate Reservoir Using an Embedded Discrete Fracture Model. Presented at the Abu Dhabi International Petroleum Exhibition and Conference, Abu Dhabi, 10–13 November. SPE-171830-MS. <http://dx.doi.org/10.2118/171830-MS>.
- Patzek, T. W., Male, F., and Marder, M. 2013. Gas Production in the Barnett Shale Obeys a Simple Scaling Theory. *PNAS* **110** (49): 19731–19736. <http://dx.doi.org/10.1073/pnas.1313380110>.
- Peaceman, D. W. 1983. Interpretation of Well-Block Pressures in Numerical Reservoir Simulation With Nonsquare Grid Blocks and Anisotropic Permeability. *SPE J.* **23** (3): 531–543. SPE-10528-PA. <http://dx.doi.org/10.2118/10528-PA>.
- Peng, D. Y. and Robinson, D. B. 1976. A New Two-Constant Equation of State. *Ind. Eng. Chem. Fund.* **15** (1): 59–64. <http://dx.doi.org/10.1021/i160057a011>.
- Sandve, T. H., Berre, I., and Nordbotten, J. M. 2012. An Efficient Multi-Point Flux Approximation Method for Discrete Fracture–Matrix Simulations. *Journal of Computational Physics* **231** (9): 3784–3800. <http://dx.doi.org/10.1016/j.jcp.2012.01.023>.
- Seldle, J. P. and Arri, L. E. 1990. Use of Conventional Reservoir Models for Coalbed Methane Simulation. Presented at the CIM/SPE International Technical Meeting, Calgary, 10–13 June. <http://dx.doi.org/10.2118/90-118>.
- Warpinski, N. R., Mayerhofer, M. J., Vincent, M. C. et al. 2009. Stimulating Unconventional Reservoirs: Maximizing Network Growth While Optimizing Fracture Conductivity. *J Can Pet Technol* **48** (10): 39–51. SPE-114173-PA. <http://dx.doi.org/10.2118/114173-PA>.
- Weijers, L. and de Pater, C. J. 1992. Fracture Reorientation in Model Tests. Presented at the SPE Formation Damage Control Symposium, Lafayette, Louisiana, USA, 26–27 February. SPE-23790-MS. <http://dx.doi.org/10.2118/23790-MS>.
- Weng, X., Kresse, O., Cohen, C.-E. et al. 2011. Modeling of Hydraulic Fracture-Network Propagation in a Naturally Fractured Formation. *SPE Prod & Oper* **26** (4): 368–380. SPE-140253-PA. <http://dx.doi.org/10.2118/140253-PA>.
- Wu, K. and Olson, J. E. 2014. Mechanics Analysis of Interaction Between Hydraulic and Natural Fractures in Shale Reservoirs. Presented at the SPE/AAPG/SEG Unconventional Resources Technology Conference, Denver, 25–27 August. SPE-2014-1922946-MS. <http://dx.doi.org/10.15530/urtec-2014-1922946-MS>.
- Wu, K. and Olson, J. E. 2015. Simultaneous Multifracture Treatments: Fully Coupled Fluid Flow and Fracture Mechanics for Horizontal Wells. *SPE J.* **20** (2): 337–346. SPE-167626-PA. <http://dx.doi.org/10.2118/167626-PA>.
- Yu, W. 2015. A Comprehensive Model for Simulation of Gas Transport in Shale Formation With Complex Hydraulic Fracture Geometry. Presented at the SPE Annual Technical Conference and Exhibition, Houston, 28–30 September. SPE-2015-178747-STU. <http://dx.doi.org/10.2118/178747-STU>.
- Yu, W., Lashgari, H. R., Wu, K. et al. 2015. CO₂ Injection for Enhanced Oil Recovery in Bakken Tight Oil Reservoirs. *Fuel* **159**: 354–363. <http://dx.doi.org/10.1016/j.fuel.2015.06.092>.
- Yu, W., Wu, K., and Sepehrnoori, K. 2016. A Semianalytical Model for Production Simulation From Nonplanar Hydraulic-Fracture Geometry in Tight Oil Reservoirs. *SPE J.* **21** (3): 1028–1040. SPE-178440-PA. <http://dx.doi.org/10.2118/178440-PA>.
- Zhou, W., Banerjee, R., Poe, B. et al. 2014. Semi-analytical Production Simulation of Complex Hydraulic-Fracture Networks. *SPE J.* **19** (1): 6–18. SPE-157367-PA. <http://dx.doi.org/10.2118/157367-PA>.

Appendix A: Derivation of Matrix–Fracture Transmissibility Factor

As shown in Fig. 2, the matrix cell is divided into two parts: A and B. We denote the volume of Part A and Part B as V_A and V_B , respectively. The average pressure in the total matrix-cell is

$$p_m = (V_A \times p_A + V_B \times p_B) / (V_A + V_B), \quad \dots \quad (\text{A-1})$$

where p_A and p_B are the average pressure in Parts A and B, respectively. We assume the same pressure gradients in A and B as shown by the red arrows. Let d_A and d_B be the average normal distances from Part A and Part B to the fracture plane. The flow rate of phase j from the Fracture Surface 1 to Part A is

$$Q_{f-A} = T_{f-A} \lambda_j (p_f - p_A), \quad \dots \quad (\text{A-2})$$

where p_f is the average pressure in the fracture segment, T_{f-A} is the phase-independent part of transmissibility between the fracture and Part A, and λ_j is the relative mobility of phase j . T_{f-A} can be calculated by

$$T_{f-A} = A_f (K \cdot \vec{n}) \cdot \vec{n} / d_{f-A}, \quad \dots \quad (\text{A-3})$$

where A_f is the area of the fracture segment on one side, K is the matrix-permeability tensor, \vec{n} is the normal vector of the fracture plane, and d_{f-A} is the average normal distance from Part A to the fracture, which can be calculated by

$$d_{f-A} = \frac{\int_{V_A} x_n dV_A}{V_A}. \quad \dots \quad (\text{A-4})$$

$(p_f - p_A) \vec{n} / d_{f-A}$ is the pressure gradient. In the case of anisotropic matrix permeability, the flow direction may be different from the direction of the pressure gradient. Therefore, the second \vec{n} in the equation projects the flow velocity onto the direction normal to the fracture plane.

Similarly, the flow rate of phase j from the Fracture Surface 2 to Part B is

$$Q_{f-B} = T_{f-B} \lambda_j (p_f - p_B), \quad \dots \quad (\text{A-5})$$

and

$$T_{f-B} = A_f (K \cdot \vec{n}) \cdot \vec{n} / d_{f-B}, \quad \dots \quad (\text{A-6})$$

$$d_{f-B} = \frac{\int_{V_B} x_n dV_B}{V_B}. \quad \dots \quad (\text{A-7})$$

The total flow from fracture to matrix is

$$Q_{f-m} = Q_{f-A} + Q_{f-B}. \quad \dots \quad (\text{A-8})$$

By the definition of T_{f-m} ,

$$Q_{f-m} = T_{f-m} \lambda_j (p_f - p_m). \quad \dots \quad (\text{A-9})$$

Assuming the same magnitude of pressure gradients on both sides of the fracture, we have

$$\frac{p_f - p_A}{p_f - p_B} = \frac{d_{f-A}}{d_{f-B}}. \quad \dots \quad (\text{A-10})$$

Combining all these equations, we can obtain

$$T_{f-m} = \frac{2A_f (K \cdot \vec{n}) \cdot \vec{n}}{(V_A d_{f-A} + V_B d_{f-B}) / (V_A + V_B)}. \quad \dots \quad (\text{A-11})$$

Notice that the denominator of Eq. A-11 is the same as the definition of d_{f-m} in Eq. 2.

Appendix B: Gas-Desorption Model and Revised PVT Table in Simulations

Seidle and Arri (1990) proposed a method to model gas desorption in a standard black-oil simulator. In their method, the gas adsorbed to the rock surface can be mathematically treated as gas

p	R_s	B_o	B_g	μ_g (cp)
14.7	201.6	0.001	0.2189	0.0129
400	3,224.5	0.001	0.0078	0.0132
800	4,516.7	0.001	0.0038	0.0136
1200	5,213.1	0.001	0.0025	0.0141
1600	5,648.5	0.001	0.0018	0.0149
2000	5,946.5	0.001	0.0015	0.0158
2400	6,163.3	0.001	0.0012	0.0168
2800	6,328.1	0.001	0.0010	0.0180
3200	6,457.6	0.001	0.0009	0.0192
3600	6,562.0	0.001	0.0008	0.0206
4000	6,648.0	0.001	0.0007	0.0219
9000	7,114.3	0.001	0.0004	0.0376

Table B-1—PVT table for the simulation.

dissolved in an immobile oil. By assuming a small oil saturation, the Langmuir gas desorption can be modeled with the solution-gas–oil ratio

$$R_s = \frac{0.17525 \nu_L \rho_B B_o p}{\phi_m S_{om} (p_L + p)}, \quad \text{..... (B-1)}$$

where ν_L = Langmuir isotherm constant, scf/ton; ρ_B = rock density, g/cm³; B_o = oil formation volume factor, assumed to be constant; p_L = Langmuir pressure, psi; p = pressure, psi; ϕ_m = reservoir porosity in this equivalent model; $\phi_m \approx \phi$ for small S_{om} ; S_{om} = assumed oil saturation; and R_s = solution gas–oil ratio, scf/STB.

In this study, we assume $B_o = 0.001$ and $S_{om} = 0.001$, and the PVT table in the black-oil model is shown in **Table B-1**.

Appendix C: A Semianalytical Model

In this study, we used a semianalytical solution to verify our model for the nonplanar fracture geometry with varying fracture aperture and fracture permeability along fracture length. The semianalytical model discretizes the nonplanar fracture geometry into a number of small fracture segments. It mainly consists of two parts for simulating shale gas production. First, an analytical solution is used to solve the diffusivity equation for gas transport in shale. Second, a numerical solution is used to solve gas flow in each fracture segment. Below, we briefly introduce the fundamental equations for gas transport in shale and gas flow in a fracture. More details about the model development and verification can be found in Yu et al. (2016) and Yu (2015).

The diffusivity equation of conventional gas reservoirs is modified by considering the gas-desorption effect for modeling gas transport in shale, as follows:

$$\left[\frac{\partial}{\partial x} \left(\frac{\rho_g k}{\mu_g} \frac{\partial p}{\partial x} \right) + \frac{\partial}{\partial y} \left(\frac{\rho_g k}{\mu_g} \frac{\partial p}{\partial y} \right) + \frac{\partial}{\partial z} \left(\frac{\rho_g k}{\mu_g} \frac{\partial p}{\partial z} \right) \right] = [S_g \phi + (1 - \phi) K_a] c_g \rho_g \frac{\partial p}{\partial t}, \quad \text{..... (C-1)}$$

where ρ_g is gas density, ϕ is rock porosity, k is reservoir permeability, c_g is the isothermal gas-compressibility factor, p is pressure, μ_g is gas viscosity, and K_a is the differential equilibrium-partitioning coefficient of gas at a constant temperature, which is a function of pressure and temperature, and defined as (Patzek et al. 2013):

$$K_a = \left(\frac{\partial \rho_a}{\partial \rho_g} \right)_{T_R}, \quad \text{..... (C-2)}$$

where ρ_a is the adsorbed-gas mass per-unit shale volume (kilograms of adsorbed gas per cubic meter of solid). In this study, we used the Langmuir isotherm to model the gas-desorption effect (Langmuir 1918),

$$v = \frac{p v_L}{p + p_L}, \quad \text{..... (C-3)}$$

where v_L is Langmuir volume and p_L is Langmuir pressure. According to the form of the Langmuir isotherm, the differential equilibrium-partitioning coefficient of gas can be expressed as

$$K_a = \frac{\rho_g (p_{ST}, T_{R,ST}) \rho_b}{c_g \rho_g (1 - \phi)} \frac{v_L p_L}{(p_L + p)^2}, \quad \text{..... (C-4)}$$

where ρ_b is bulk density of shale and $\rho_g (p_{ST}, T_{R,ST})$ is the stock-tank gas density. The analytical solution for the previously modified diffusivity equation can be found in Yu et al. (2016) and Yu (2015).

For gas flow in the fracture, the pressure drop along the j th fracture segment is proportional to the fluid velocity, and can be calculated as follows:

$$p_i - p_{j+1} = \int_{y_j}^{y_{j+1}} \left(\frac{\mu_g}{\rho_g k_f w_f h_f} \right)_j [q_j + q_{fj}(y - y_j)] dy, \quad \text{..... (C-5)}$$

where k_f is fracture permeability, w_f is fracture aperture, h_f is fracture height, q_j is gas-flow rate at the node j of the j th fracture segment, and q_{fj} is the flux of the j th fracture segment.

In addition, the mass balance is satisfied for each intersection point of fracture segments.

SI Metric Conversion Factors

cp × 1.0	E-03 = Pa·s
days × 8.64	E+04 = seconds
ft × 3.048	E-01 = m
°F (°F-32)/1.8	= °C
°F (°F+459.67)/1.8	= K
lb/ft ³ × 1.6018	E+01 = kg/m ³
mdm × 9.869	E-16 = m ²
psi × 6894.757	E+00 = kPa
scf × 2.831	E-02 = m ³
STB × 1.5899	E-01 = m ³
ton × 9.072	E+02 = kg

* Conversion factor is exact.

Yifei Xu is a PhD student in the Department of Petroleum and Geosystems Engineering at the University of Texas at Austin. His research interests include development and application of reservoir simulators for naturally fractured reservoirs, hydraulically fractured reservoirs, and unconventional resources. Xu holds a BS degree in thermal engineering from Tsinghua University in China and an MS degree in petroleum engineering from the University of Texas at Austin. He is a member of SPE.

Jose Sergio de Araujo Cavalcante Filho is a reservoir engineer working with Petrobras. He works with presalt reservoirs in Brazil, and his research interests include reservoir modeling and simulation of heterogeneous and fractured reservoirs, mobility

control, and carbon-dioxide enhanced oil recovery (EOR). Cavalcante Filho holds a BS degree in mechanical engineering from Federal University of Ceara in Brazil, an MS degree in petroleum engineering from State University of Campinas, and a PhD degree in petroleum engineering from the University of Texas at Austin. He is an active member of SPE.

Wei Yu is a research associate in the Harold Vance Department of Petroleum Engineering at Texas A&M University. His research interests include reservoir modeling and simulation of shale gas and tight oil production, carbon dioxide EOR in tight oil reservoirs, and nanoparticles EOR. Yu has authored or coauthored more than 50 technical papers and holds one patent. He holds a BS degree in applied chemistry from University of Jinan in China, an MS degree in chemical engineering

from Tsinghua University in China, and a PhD degree in petroleum engineering from the University of Texas at Austin. Yu is an active member of SPE.

Kamy Sepehrnoori is a professor in the Department of Petroleum and Geosystems Engineering at the University of Texas at Austin, where he holds the W. A. (Monty) Moncrief Centennial Chair in Petroleum Engineering. His research interests and teaching include computational methods, reservoir simulation, parallel computing, EOR modeling, naturally fractured reservoirs, and unconventional resources. Sepehrnoori is the director of the Reservoir Simulation Joint Industry Project in the Center of Petroleum and Geosystems Engineering. He holds a PhD degree from the University of Texas at Austin. Sepehrnoori is a member of SPE.